

RAM

● ROBOTICS
AND
MECHATRONICS

CONTROL AND EX-VIVO EVALUATION OF SUNRAM 7: AN MR SAFE ROBOTIC SYSTEM FOR BREAST BIOPSY

H. (Harsh) Ranjan

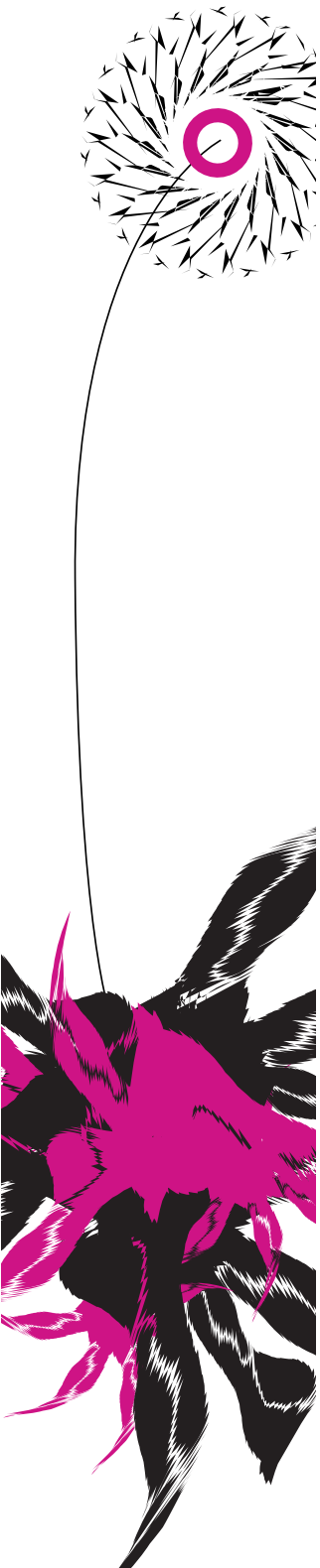
MSC ASSIGNMENT

Committee:

prof. dr. ir. S. Stramigioli
dr. V. Groenhuis, MSc
dr. F.J. Siepel
dr. ir. W.M. Brink

August, 2022

040RaM2022
Robotics and Mechatronics
EEMCS
University of Twente
P.O. Box 217
7500 AE Enschede
The Netherlands



Summary

Diagnosis of one of the most dangerous and threatening diseases in woman, breast cancer, creates a crucial risk to the patients if it is not screened, diagnosed and treated at the early stages. MRI guided breast biopsy is recommended if the lesions are too small to notice or to confirm any previous diagnosis. To accurately sample the lesion tissues, prevent high tissue damage and reduce the procedural time, thus costs, the Sunram 7 is designed & fabricated at RAM, and evaluated in free air and in the MR environment. It is a 5 DOF, MR safe robot which can perform MR guided breast biopsy using a hollow needle-like biopsy gun. Its positioning and targeting errors were studied in free air and lesion mimicking stiff coloured PVC structures inside a breast phantom were targeted, to obtain tissue samples using the 0.25T Esaote scanner, while identifying the different error sources in the system. Upon building the pre-requisites and conducting the initial studies with respect to the segmentation and transformations, the Sunram 7 was evaluated to be labeled accurate, with maximum mean positioning error of $3.18 \pm 0.8 \text{ mm}$ in the 3D space ($0.3 \pm 1.6 \text{ mm}$, $1.9 \pm 0.8 \text{ mm}$ and $1.5 \pm 0.95 \text{ mm}$ in x, y and z directions respectively). The Sunram 7 could obtain coloured biopsy samples, with a success rate of 70% in the MR environment. Comparing with the standard manual breast biopsy process, this robotic system displays potential to perform MR guided breast biopsy, inside the MR scanner's bore by reducing time, tissue damage and eliminating movement errors due to in-situ operation.

Contents

Summary	ii
List of acronyms	ix
1 Introduction	1
1.1 Screening & Detection	1
1.2 Clinical Challenges	2
1.3 Motivation	2
1.4 Framework and goals	3
1.5 Experiments and Evaluations	4
1.6 Report organization	4
2 Literature review	5
2.1 Breast Imaging Techniques	5
2.1.1 Mammography	5
2.1.2 Ultrasound	7
2.1.3 Magnetic Resonance Imaging	8
2.1.4 Other Imaging Techniques	9
2.2 Breast Biopsy Procedure	11
2.3 MR compatibility	13
2.4 State of the Art	14
3 Sunram 7	21
3.1 Components & Design	21
3.2 Kinematic Model	25
3.2.1 Forward Kinematics	25
3.2.2 Inverse Kinematics	26
3.3 Work Volume	27
3.4 Interface	28

4	Method & Experiments	30
4.1	Research Methodology	30
4.2	Segmentation & Localization	31
4.2.1	Breast phantoms	31
4.2.2	MRI scanner and scan sequences	31
4.2.3	Segmentation	32
4.2.4	Localization	33
4.3	Registration & Transformation	33
4.4	Joint actuation	35
4.5	Needle positioning accuracy - in air	36
4.6	Needle targeting accuracy - in air	36
4.7	Accuracy evaluation - MR environment	37
5	Experimental Results	40
5.1	Segmentation	40
5.2	Transformation	40
5.3	Joint actuation	44
5.4	Needle positioning accuracy - in air	44
5.5	Needle targeting accuracy - in air	47
5.6	Accuracy evaluation - MR environment	49
5.7	Comparison with standard biopsy process	51
5.8	Discussions	53
6	Conclusions and recommendations	57
6.1	Conclusions	57
6.2	Recommendations	58
	Bibliography	60
	Appendices	
A		68
A.1	Breast phantoms	68
A.2	MRI scanning sequences	69
A.3	Segmentation	69
A.4	Homogeneous transformation matrix	71
A.5	Interface circuit	72
A.6	Sunram 7 system	73
A.7	Needle targeting - in air : Setup and output	74
A.8	Accuracy evaluation - MR environment	75

List of Figures

2.1	Different breast cancer imaging techniques	6
2.2	Left: A typical mammography procedure [1]. Right: A Mammogram - (a)&(b) CC view,(c)&(d) MLO view [2]	7
2.3	Left: A typical ultrasound procedure [3]. Right: Ultrasound scans of healthy and cancerous breast [4]	8
2.4	Left: A standard breast MRI imaging procedure. Right: MRI of a breast [5]	9
2.5	Top: (a)Breast MRI and (b)PET scan [6]. Bottom: SPECT scans [7] . .	10
2.6	Optical spectroscopy of breast blood concentration [8]	10
2.7	Ultrasound guided breast biopsy procedure	11
2.8	Patient inside a MRI scanner [9]	12
2.9	The MR safety markings [10]	14
2.10	Breast intervention robot by Zhang <i>et al.</i>	15
2.11	Dimensions and prototype of the robotic system by Navarro-Alarcon <i>et al.</i>	15
2.12	Bendable needle structure and manipulator design - Park <i>et al.</i> [11] .	16
2.13	Left: Master robot. Right: Slave robot - Yang <i>et al.</i> [12]	16
2.14	Positioning device(left) and a device overview(right) - Larson <i>et al.</i> [13]	17
2.15	Left: Stewart platform. Right: Stormram 1	17
2.16	Left: Stormram 2. Right: Stepper motor	18
2.17	Left: Stormram 3. Right: T-49 pneumatic stepper motor	19
2.18	Left: Stormram 4. Right: C-30 curved pneumatic stepper motor	19
2.19	Left: Sunram 5 and its joints(J) and cylinders(C). Right: (a)Linear stepper motor,(b)Curved stepper motor,(c)novel dual-speed stepper motor	20
3.1	Stages of cylinder(A,B) actuation for one-tooth-displacement of the gear(G)	22
3.2	Sunram 7 CAD and real robot at zero (home) position	23
3.3	Sunram 7 CAD and real robot at the maximum allowed position	24
3.4	The 8 different fiducial markers in the Sunram 7 base frame (F1 - F8)	24

3.5	Sunram-7 CAD, with the frames assigned as per D-H convention (from frame {1} for joint 1 to frame {6} for the needle-tip)	25
3.6	The 3D reachable workspace of the Sunram 7	28
5.1	Segmentation error for all markers	41
5.2	All markers on the Sunram 7	42
5.3	Transformation algorithm comparison : actual vs transformed marker positions	42
5.4	Comparison of transformation algorithms based on the TRE for two targets	43
5.5	Obtained joint actuation displacements with image processing toolbox in MATLAB, for joint 1 (J1) to 5 (J5)	45
5.6	Displacement of setpoint position in x axis vs positional error	46
5.7	Displacement of setpoint position in y axis vs positional error	46
5.9	Elevation angle about x axis vs positional error	47
5.8	Insertion angle about z axis vs positional error	47
5.10	Targeting error along x and z versus target coordinate displacement in x axis	48
5.11	Targeting error along x and z versus target coordinate displacement in y axis	48
5.12	Targeting error along x and z versus target coordinate displacement in z axis	49
5.13	Different possible sources of error	55
A.1	Different breast phantoms	68
A.3	3D Slicer window containing the segmented breast phantom, lesions, 8 fiducial markers(blue) and 5 target markers(3 x tall-red,2 x short-pink/magenta)	69
A.2	Different MRI scanning sequences	70
A.4	Left: The power management circuit design. Right: Soldered circuit board with TIP120 transistors	72
A.5	Controller designed for Sunram 7	73
A.7	Left: Long and short markers for TRE. Right: target pillars for tests	73
A.6	The complete Sunram 7 system	74
A.8	Setup: To study Sunram 7's needle targeting accuracy in free air - Before insertion(left), during insertion/targeting(center) and after making a hole at the target location(right)	74
A.9	Target sheets, at three different y planes, with 'punctures'	75
A.10	Sunram 7 and breast phantom setup inside the MR room	76
A.11	Biopsy sample outputs for 3 lesions	77

A.12 The red attachment designed to prevent needle bending 77

List of Tables

3.1	Sunram 7 joint specifications	23
3.2	D-H parameters of Sunram 7	26
5.1	Transformation algorithm vs fiducial localization error, in the robot coordinate frame ψ_B	43
5.2	Consolidated results from the breast phantom biopsy tests	50
5.3	Mean positioning error and standard deviation in each axis, and the mean 3-D distance between measured needle tip position and actual target location	54
5.4	Mean targeting error in x and z axis, with the mean 2-D offset between measured target position and the actual target coordinates	55

List of acronyms

MRI	magnetic resonance imaging
RF	radio frequency
EU	European Union
2D	two-dimensional
3D	three-dimensional
MLO	mediolateral oblique
CC	bilateral craniocaudal
RAM	Robotics and Mechatronics

Introduction

Oncogenesis or carcinogenesis, which is mainly distinguished by six hallmarks, is the transformation of healthy cells into cancer cells, which can occur in any tissue or organ, and leads to various pathological modification [14]. Progression of such transformations is assisted by different mechanisms such as endless division capacity, magnified angiogenesis, elusion of apoptosis and the ability to metastasize. This results in a large number of cancer-related risks, as 19.3 million cancer cases worldwide (excluding nonmelanoma skin cancer) were estimated by GLOBOCAN data in 2020 [15].

To date, breast cancer extensively remains the most commonly diagnosed malignancy amongst women, contributing to 2.3 million new cases (11.7% of total cases in 2020), surpassing lung and prostate cancer (11.4% and 7.3% respectively) [15].

These statistics, previous studies [16] and WHO [17] clearly imply that early stage detection of breast cancer, coupled with improved & suitable treatment methods, can notably reduce death rates in the long run - which resonates equally well with radiologists, clinicians and patients.

1.1 Screening & Detection

Screening is defined as a precautionary, periodic check-up of the organ (breasts) for any signs of cancer, prior to any symptoms or signs showing up [18]. In The Netherlands, the national screening program for breast cancer, was started in 1988. In this, woman between the age of 50 and 75 are invited every two years to take part in the screening process [19]. This helps with early detection of any signs of cancer, so it can be prevented and treated early and in time. The screening process involves a diagnosis step in which some imaging/detection technique is used to view the region of interest. Usually, a mammography is recommended by the European Society of Breast Imaging [20]. But the sensitivity and diagnostic

accuracy of mammography is relatively restricted [21]. Thus, different modalities can be considered, in consultation with a radiologist, who is directly liable to the patient. Ultrasound, elastography, CT, PET and MRI are some of the other techniques which are used for diagnosis purposes [22].

1.2 Clinical Challenges

If suspicious tissue is observed, which needs further examination, a biopsy process has to be carried out, using an imaging modality for visualization, localization and guidance. The National Cancer Institute defines a biopsy process as the "removal of cells or tissues for examination by a pathologist" [23]. In this step, a cylindrical volume of tissue is extracted by inserting a hollow biopsy needle at the region of interest - which is then sent for histopathological diagnosis.

The challenge arises when techniques, like the mammography, ultrasound and other modalities, do not show any suspicious tissues or lesions, as they can only be visualized in an magnetic resonance imaging (MRI) procedure. Due to its very high sensitivity, MRI modality is commonly used for the screening process in high-risk patients. But due to its low specificity, it is often accompanied by the aforementioned biopsy process.

MRI guided biopsies are time consuming and expensive procedures, with varying precision - owing to the requirements of acquiring multiple scans, moving patients in and out of the MRI bore and performing multiple inserting (if the needle failed to reach the target). Here, the radiologist first reads many previously acquired MRI scans of the patient, determines where the tissue/lesion is, positions and inserts the needle using the grid or pillar or post positioning system [24]. This procedure takes place outside the MRI bore due to obvious space constraints and limitations. The patient is then pushed back into the scanner for a post biopsy scan to confirm the extraction process. If the needle is unable to target the lesion accurately, as it is dependant on the freehand insertion experience of the radiologist, the patient is taken out from the bore to re-insert the needle and perform the biopsy again. Not only is this time consuming, it is also coupled with increased tissue damage.

1.3 Motivation

The established standard procedure for biopsies using the MRI modality depends on the freehand alignment and intervention, with no supervision and control of the needle tip's end position. In addition, the limited and ergonomically challenging workspace places a hard constrain that any procedure should take place outside the

bore. This means the patient has to be taken in and out of the bore multiple times during the entire procedure. Breathing pattern of the patient, random vibrations and other forces in play could cause unnecessary displacements in tissue, lesions and the breast, which would then need a re-targeting and biopsy [25].

Thus, there clearly arises a need of a MRI compatible system which can operate and accurately perform biopsies inside the bore, aimed at reducing the total procedure time and minimising tissue damage. An MRI compatible robotic system would make the needle tip positioning more precise and increase lesion targeting accuracy, without affecting the sensitivity of the MRI machine or the scanned image quality. Accurate biopsy would in turn reduce repeated needle insertions, thereby reducing tissue damage and procedure time.

1.4 Framework and goals

The Robotics and Mechatronics (RAM) group at University of Twente have developed multiple MRI compatible and assisted robotic systems for breast biopsies. Sunram 7 is the the 7th iteration of the robot, which is the proposed solution to the above mentioned shortcomings. It is a 5 DOF serial manipulator, actuated by pneumatic stepper motors designed by Groenhuis *et. al* [26] using compressed air. Thus, controlling the positioning of the robot, needle insertion and tissue extraction processes - displaying capabilities to perform in-situ clinical breast biopsies.

The aim of this study is to compare the standard manual biopsy process with that developed using the Sunram 7, and evaluating the operating time and accuracy of the biopsy process. Before starting with the assessment of the robot, a few key assistive components must first be studied and established. These include pre-operative MRI scans for robot registration in the MR coordinate frame & lesion localization and developing a forward and inverse kinematic model to monitor, test and control the Sunram 7. Once these are sufficiently implemented, the Sunram 7 will then be evaluated for its needle positioning and targeting accuracy, in free air and for its targeting accuracy in the MRI environment using a breast mimicking phantom. This leads to the following research questions :

- How do we localise the robot in the scanner's coordinate frame, and obtain lesion coordinates in the robot frame, using MRI technique?
- How accurately does the Sunram 7 position the needle and perform biopsies?
- What are the different sources of error in the entire robot assisted biopsy process?

- How does the biopsy procedure time with Sunram 7 compare with the current standard manual breast biopsy procedure?

1.5 Experiments and Evaluations

To answer the research questions stated in section 1.4, a set of tests and experiments were carried out. The experiments are broadly categorized into two - free air (in-air) tests and tests in the MR environment with a breast phantom. The evaluation of the robot is monitored in terms of its positioning and targeting accuracy.

Tests in air include joint actuation and verification tests, needle positioning tests using pre-defined target coordinates and needle targeting tests using a "target grid" sheet with multiple targets, such that the needle insertion results in a hole or puncture at the target location. To begin with the experiments in the MR environment, MRI scans of the breast phantom and Sunram 7 were taken. Once the lesions are identified, transformed and localized, the Sunram 7 is then directed towards the target to perform the biopsy process.

The comparison between standard manual process and that, developed with the Sunram 7, is based on the procedure time of each process. The results from the tests are documented and analyzed. Conclusions and discussions are drawn from the entire study and elaborated in this report.

1.6 Report organization

This report examines and summarizes all the key findings from past studies and the results obtained while extensively studying the Sunram 7. Chapter 2 looks into all related theory, framework and past studies conducted within the scope of this research. It highlights the different medical terminologies, biopsy processes, comparison of other MR compatible robotic systems and other relevant pieces of information. Chapter 3 then dives into the details of Sunram 7. It includes comprehensive details about the pneumatic actuators used, the mechanical design and the operating workspace. Chapter 4 contains all the materials and methods used in this study, how they are translated to various experiments and how it's implemented and evaluated. The experimental results obtained are then highlighted and extensively discussed in Chapter 5. Finally, the conclusion, recommendations and future scope are discussed in Chapter 6.

Literature review

This chapter covers the intensive overview of the past studies and literature undertaken in the field of MRI guided biopsy and state of the art robotic systems developed for the same. As this research revolves around a robotic system developed for breast biopsy, the literature is centered around breast imaging techniques, breast biopsy and MRI compatible breast biopsy robotic systems.

2.1 Breast Imaging Techniques

As discussed in Chapter 1, although there is not one clear cause of breast cancer, mortality rates in the European Union (EU) and North America have dropped, largely owing to the early screening and detection processes, as it enhances survival rates by 5 years [27]–[29]. For the purpose of finding and examining breasts, which may contain questionable lesions or tumors, there exists a variety of two and three dimensional imaging techniques. They can broadly be categorized into 5 groups, as shown in Fig 2.1. The easiest non-imaging modality is known as Palpation. It is defined as the examination of the organs(breast) and the tissue underneath, by feeling and pressing on the surface with the fingers, palm or hands, thereby analyzing stiffness, texture, size and location [30] [31]. Here, one hand palpates the breast, while the other stabilizes and confines the breast. This is the most primitive diagnostic method and can even be used for self assessments. But due to its low sensitivity and dependency on large tumour sizes up-to a certain depth, this technique can only be limited to very early self assessment and preliminary check-ups. Thus, other imaging modalities are needed for better detection and thorough evaluation.

2.1.1 Mammography

Mammography is the golden standard in breast cancer imaging, which utilizes low energy x-rays to render a mammogram - a two-dimensional (2D) gray-scale image

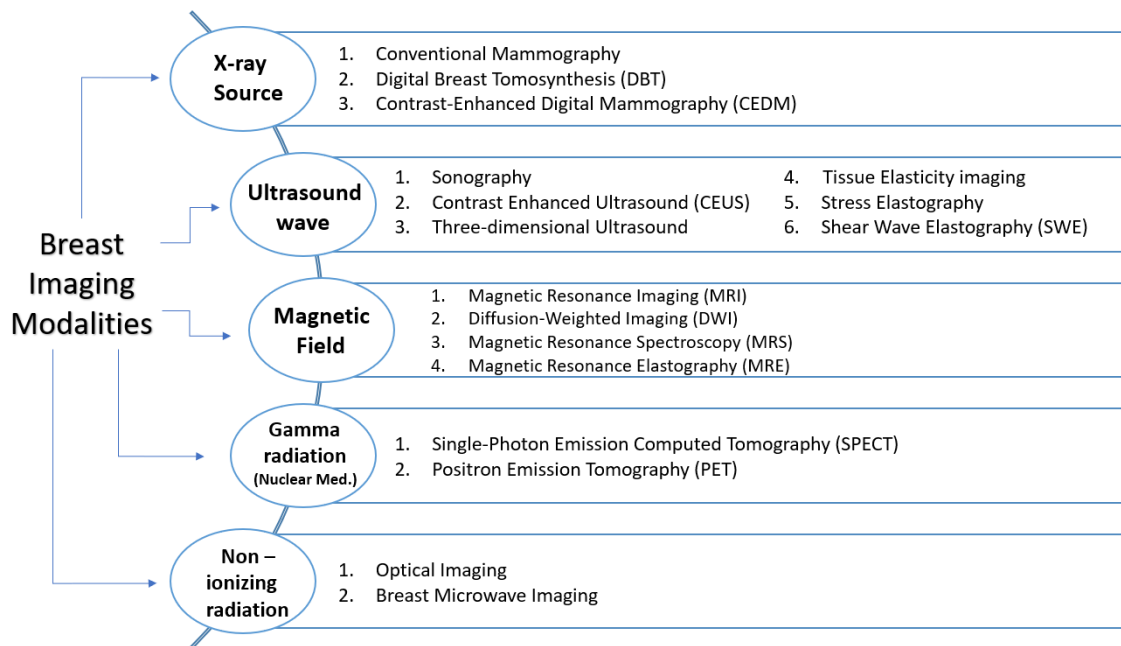


Figure 2.1: Different breast cancer imaging techniques

which captures the various intricacies of the breast and morphologically doubtful tumours or discoveries, if present. These can include masses, asymmetrical calcifications and deformed areas [8].

In this technique, the breast is compressed by two plates, which is horizontally aligned with respect to the person standing (as shown in Fig 2.2(left)). The 2D mammogram is obtained by then passing low-energy x-rays (20-32 kVp) into the breast tissues. The imaging of the breast is generally represented in two views - the mediolateral oblique (MLO) view, which is the "top-down" view and the bilateral craniocaudal (CC) view, the side view which is usually at an angle, as shown in Fig 2.2(right).

There exists an inverse relationship between the sensitivity of the mammography and the density of the breast [32]. So, dense breasts result in non-optimal imaging. As mammograms are a 2D image, it is relatively easier to miss details in the direction normal to the plane of the image. Due to these reasons, the sensitivity of mammography is limited to about 62% in women, who are aged between 40 and 49, and it ranges between 68% and 90% in women aged 50 or above. Specificity of this imaging modality ranges from 82-97%. [33]. Due to the overlapping of fibroglandular tissues and stray appearance of cancer-resembling abnormalities, mammography has a high false positive rate.

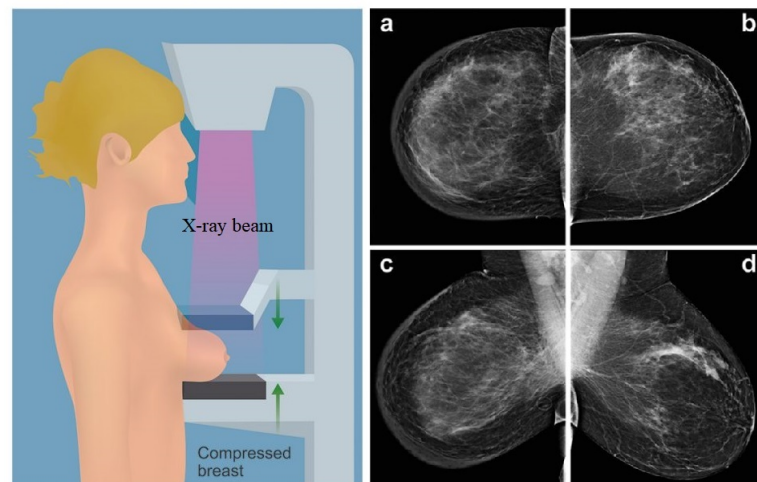


Figure 2.2: Left: A typical mammography procedure [1]. Right: A Mammogram - (a)&(b) CC view,(c)&(d) MLO view [2]

2.1.2 Ultrasound

The ultrasound imaging modality, also known by the term 'ultrasonography', exploits the reflection of high frequency acoustic waves from different organs and tissues due to their differences in acoustic impedance [8]. The frequency of the waves range from 3-12MHz, which is generated either by single piezoelectric wafers or an array of such wafers, is transmitted via a handheld probe [34]. This probe presses and slides over the surface of the breast, while transmitting waves and receiving attenuated waves, and generates a real time 2D image of the breast based on the difference of the attributes of the transmitted and received attenuated acoustic wave.

Fig2.3(left) displays a standard breast ultrasound scanning process. As the probe is a free-to-move transducer, the imaging plane is arbitrary, thus giving the radiologist the freedom to image any section of the breast in a orientation the radiologist prefer. This helps for better analysis of various characteristics, from different points of view.

Fig2.3(right) shows us three different ultrasound scans of the breast - normal, with benign tumour and with malignant tumour. The exposure to radiations and the low sensitivity of mammogram in denser tissues is absent in this modality, but the depth of the scan is limited to couple of centimeters - based on the acoustic wave's wavelength. Compared to the MRI(section 2.1.3) modality, ultrasound and mammography have a combined sensitivity of 44% [35]. So there might still exists lesions or tumors which can go undetected in the ultrasound imaging technique.



Figure 2.3: Left: A typical ultrasound procedure [3]. Right: Ultrasound scans of healthy and cancerous breast [4]

2.1.3 Magnetic Resonance Imaging

With practical advancements and measurable success in surface coil technology, and with introduction of newer contrasting agents, magnetic resonance imaging (MRI) has turned into a reliable and widely used imaging technology [8]. It generates three-dimensional (3D) images of the breast, exploiting the magnetic properties of the protons (hydrogen atoms) present in the breast tissues. The MRI scanner orients the angular momentum of the protons along the magnetic field introduced by the scanner. The fast oscillating electromagnetic breast coils then induce a stray magnetic field, which alters the alignment and phase of the protons with respect to the uniform magnetic field created by the scanner. Upon turning off the oscillations, the hydrogen atoms rotate back to re-orient themselves, their spins, with respect to the uniform field. This property enables us to measure their magnetic moment and the emitted radio frequency (RF). If the proton in a tissue returns to its original state fast (low T1 relaxation time), it would show up the brightest in a T1-weighted scan [36]. By applying different gradients in the scanner's magnetic field, 2D slices are defined which inscribes the position information. Within those slices, frequency and phase encoding algorithms can provide information of the rows and columns. Figure 2.4

In this imaging procedure, the patient is moved inside the MRI bore/tunnel (Fig 2.4(left)). Based on the scan requirements and the radiologist's analysis, multiple scans can be obtained using different sequences, while the patient lays in a prone position inside the scanner tunnel. A contrasting agent can also be added to enhance certain regions in the image. The MRI imaging modality has the highest sensitivity (100%) when compared to ultrasound and mammography combined. [35]. And unlike mammography, MRI does not generate any ionizing radiations.

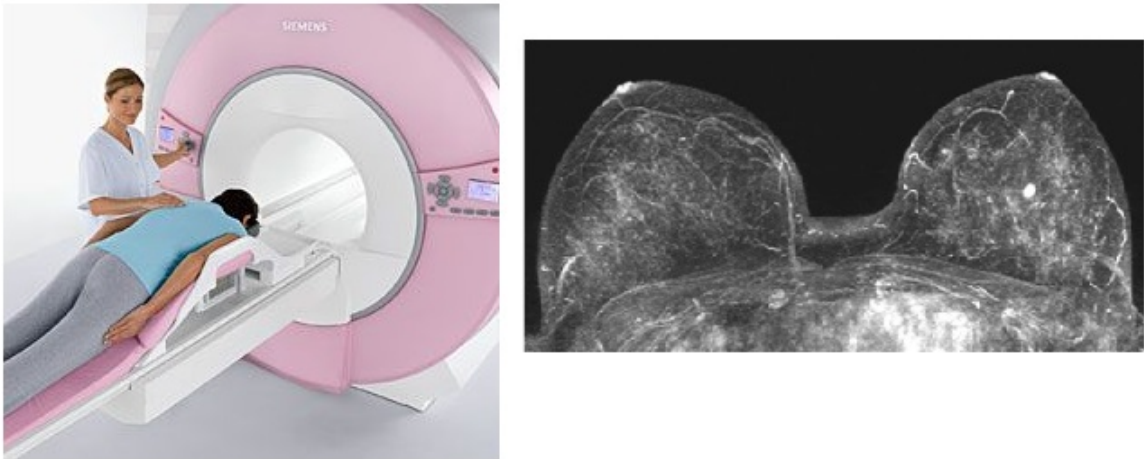


Figure 2.4: Left: A standard breast MRI imaging procedure. Right: MRI of a breast [5]

In accordance to the applied guidelines by the American College of Radiology(ACR), if a highly suspicious lesion or any malignant lesion categorized as BI-RADS 3 or above, a biopsy process is recommended which can be performed using any suitable imaging modality [37]. But if the lesion can only be identified using the MRI modality, or needs another assessment after using previous imaging techniques, then an MRI-guided breast biopsy is warranted.

2.1.4 Other Imaging Techniques

As shown in figure 2.1, there exists other imaging modalities that can be used to scan a breast. This section highlights some of the important aspects of a few other procedures.

In nuclear medicine imaging, a set of radiopharmaceuticals are introduced into the patient through their blood network and the organ specific drug intake is monitored. Positron Emission Tomography (PET) and Single-Photon Emission Computed Tomography (SPECT) are two such types. SPECT technique monitors the gamma emissions produced from activated mitochondria in the lesions, but has low spatial resolution and high false negative rates [38]. PET on the other hand monitors the gamma rays produced by the combination of a positron (injected tracer) and electron (from the increased glucose consumption by the lesions), and generates the breast scan [8]. Figure 2.5

Any imaging technique, which utilizes non-ionized infrared, ultraviolet and/or visible waved, are categorized under optical imaging. Exploiting the absorption, fluorescence and scattering properties of near-invisible (NIR, $0.7\mu\text{m} - 1\mu\text{m}$) and visible light ($0.4\mu\text{m} - 0.7\mu\text{m}$) [39]. But the biggest drawback is the penetration depth of light

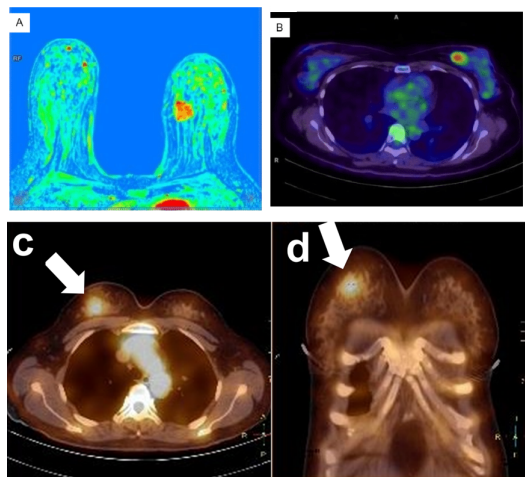


Figure 2.5: Top: (a)Breast MRI and (b)PET scan [6]. Bottom: SPECT scans [7]

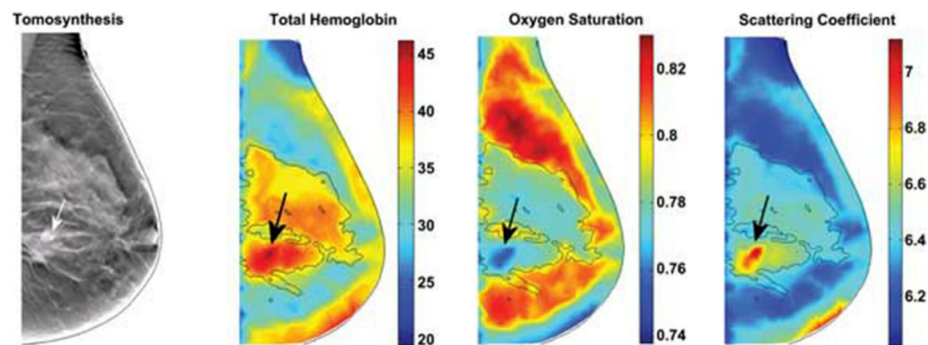


Figure 2.6: Optical spectroscopy of breast blood concentration [8]

in the tissues. Figure 2.6 depicts the optical imaging scans.

For penetration in soft breast tissues, microwave imaging utilizing electromagnetic waves with wavelength larger than infrared light and shorter than radio waves (between 1mm and 300mm). Biosensor array, size and number of sensors per array determine the quality of the microwave image produced. Widely used radar based microwave imaging measures the dielectric characteristics of the breast tissues to map the internal structure. Microwave imaging based scan resolution is directly dependant on the shortest wavelength of the radiation, i.e shorter wavelength produce finer details but at the cost of low penetration depth [8].

In any imaging techniques, if any suspicious lesions is detected or needs pathological evaluation, a biopsy process is carried out - to target lesions and extract a sample tissue from the region of interest for malignancy test.

2.2 Breast Biopsy Procedure

Derived from Greek literature, biopsy (bio - life; opsia - to see) process is defined as the removal or extraction of tissues for diagnostic and microscopic evaluations [40]. The primary goal of the biopsy process is to confirm, manage and decide on the radiographic lesion diagnosis & treatment. The current biopsy process either involves a vacuum-assisted device, which are equipped with 9 to 14 gauge needles with cutting edges. Or the biopsy process can also be carried out with a hollow needle, with a stylet and cutting cannula sliding over the stylet. A needle insertion and firing process results in cutting and extraction of the tissue [41].

Ultrasound guided breast biopsy, the high frequency transducer probe is used to scan the breast, while concomitantly inserting the needle in real time. The ultrasound scan images on the monitor acts as a visual feedback to the radiologist, who has to monitor the needle tip at all times to mentally visualise the trajectory and the surrounding environment. Upon reaching the target, the handheld biopsy device is used to cut and extract tissues from the breast. Even though it is widely used, they are user dependant and difficult to perform on smaller lesions, not to mention the undetected lesions which cannot be biopsied under ultrasound [42]. Figure 2.7(left) shows a standard ultrasound guided breast biopsy [43] and figure 2.7(right) shows the needle inserted into a 36 year-old woman [44].



Figure 2.7: Ultrasound guided breast biopsy procedure

A MRI guided breast biopsy is carried out when a lesion can only be imaged with a MR scanning sequence or if the lesion classified as BI-RADS 4 or higher [37]. The steps involved in the MRI guided breast biopsy procedure is as follows [45], [46] :

- The patient is made to lay down on a move-able exam table(as shown in figure 2.8 and a breast coil, which has cavities for the breast to be inserted into.
- An intravenous (IV) line is inserted and the patient is injected with a contrast material (such as gadolinium), for better MRI visibility, and taken into the MR scanner's bore.

- Two compression plates are then made to gently compress the breasts. One of the plates encompasses a grid structure.
- Multiple scans are then taken in succession, to compare them with the MRI scans taken before the procedure, to help locate the lesions position.
- Using the MRI scans, the lesion position with respect to the marker in the grid plate is calculated by the software, and thereby calculating the needle insertion point and depth.
- The patient is then taken out of the MR scanner's bore, to perform the biopsy process.
- A stylet, followed by the needle guide is inserted into the guide plate, at the grid position provided by the software.
- The stylet on the inside is removed and an obturator is inserted, within the needle guide.
- The patient is then again taken inside the MR scanner's bore for a tip location confirmation scan. *If* the tip is not at the required spot, the patient is taken out of the MR bore and the steps are repeated again.
- Once at the right position, the patient is taken out of the bore again, to insert the needle into the needle guide.
- Multiple tissue samples are then taken using a vacuum-assisted system.
- A small bio-marker is then placed at the biopsy site for future scans and diagnosis. A placement confirmatory scan might also be taken.
- Once everything is in order, the guides and plates are removed, any resulting wound is cleaned and pressure is applied to stop the bleeding, if any.



Figure 2.8: Patient inside a MRI scanner [9]

The MRI-guided breast biopsy is a tedious process, where the patient needs to be taken out and reinserted into the MR scanner's bore multiple times, as the insertion process can only take place outside the space-constrained bore. The patient spends most of the procedure time inside the MRI scanner, and these movements of the exam bed can induce positional errors. Not to mention, even though the grid system compresses the breast, involuntary movement, muscle actions, breathing and tissue-needle interaction can induce inaccuracies. Even the grid system induces a discretization error of around 3mm, which comes close to the order of smaller lesion size (5mm) [45]. These limitations and drawbacks are commensurated with relatively large tissue masses/samples, with thick needles, which result in high tissue damage. Therefore, there exists a need for a more accurate and efficient robotic system which is compatible and can operate inside the MRI scanner's space confined bore and perform precise biopsies

2.3 MR compatibility

Before getting into the robotic systems for MRI-guided biopsies, the term MR compatible must be understood as this constructs the basis on which the robotic system is designed and actuated. Any system which operated within the MR environment should be safe and compatible with the MRI, should be able to actuate and perform tasks while allowing for imaging at the same time, and must minimize any imaging artifacts while causing least harm to the patient due to any interactions [47].

In the MR environment, the electrical and magnetic susceptibility of the materials used in the system, which operated inside the MR bore, determines the MR safety of the system. MR safe implies that the system/device should not harm the patients, the operators and cause any damage to the MR scanner equipment [48]. Since the definition of MR safety is usually categorized with respect to variables such as orientation and position of the device and/or distance from the region of scanning, there exists a definition of categorization of devices as either *MR safe*, *MR conditional* or *MR unsafe* [49].

As shown in figure 2.9, MR safe systems must be completely free of any and all metallic components. The material used to make the system, including all miscellaneous parts, should be non-conductive (such as plastic, ceramic, fiberglass or rubber), non-metallic and non RF-reactive. Regardless of the scanning sequence, field strength or gradients, the safety of MR safe devices must be equally safe. MR conditional implies that the device or implant is safe in the MR environment under particular tested conditions which are mentioned beforehand (i.e, magnetic field strength, gradient, averaged specific absorption rate). MR unsafe includes magnetic or metallic items, which pose a danger in any and all MR environment [50].




	<p>MR safe An item which is marked MR safe poses no known hazards in all MR environments.</p>
	<p>MR unsafe An item marked MR unsafe is known to pose hazards in all MR environments.</p>
	<p>MR conditional Items marked MR conditional pose no known hazards in specified MR environments with specified conditions of use. For example, an item may be safe near a 1.5 T magnet, but not for 3.0 T.</p>

Figure 2.9: The MR safety markings [10]

MR safety now also encompasses compatibility, which implies that not only should the system be safe to the subject, operator or the scanner, it must also have minimal (ideally null) effect on the imaging quality or sequence parameters (electromagnetic pulses and static magnetic fields). In terms of the magnetic field homogeneity inside the region of interest, any system's magnetic field, generated by the driving current (if any), should not alter the uniformity of the magnetic field.

Keeping all the above stated classifications in mind, different MR safe or MR conditional mechatronic/robotic systems are developed to tackle the breast biopsy process, using the MR imaging modality.

2.4 State of the Art

To be MR safe and compatible, the robotic systems must be actuated in non-conventional actuation methods as the electromagnetic motor cannot be used inside the MR tunnel. Zhang *et. al* [51] designed a five DOF for MR guided breast biopsies. 3 of those degrees of freedom are for the x,y and z axis directions motion of the needle guide. There are two DOF more - one which acts as a puncturing module and the other which is designed for obstacle avoidance (using the grid plates). The robot also contains a storage module to collect the biopsy/tissue samples. It is made up of MR compatible materials such as non magnetic stainless steel, nylon and polyethylene and the joints are actuated using flexible shafts connected to stepper motors, which are placed outside the MR bore to maintain the robot compatibility. Navarro-Alarcon *et al.* [52] fabricated a compact breast biopsy robot capable of performing both lateral and frontal needle insertion, within the MR bore. It consists of non-magnetic slides, made from graphite, silicon nitride and aluminium). The power in the x-axis

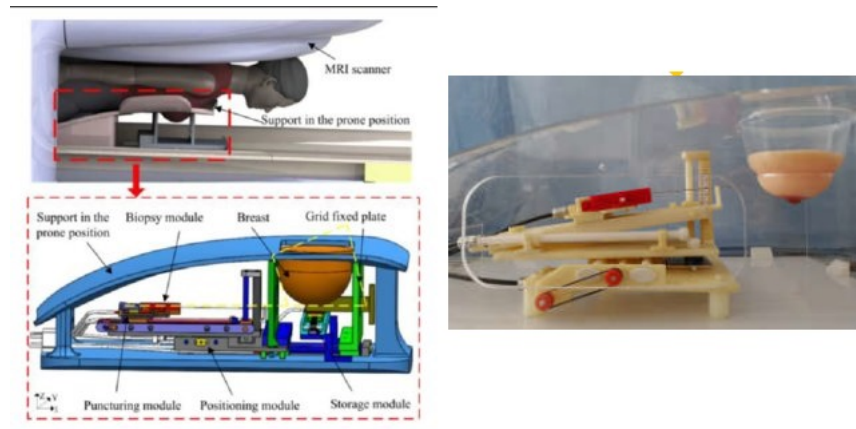


Figure 2.10: Breast intervention robot by Zhang *et al.*

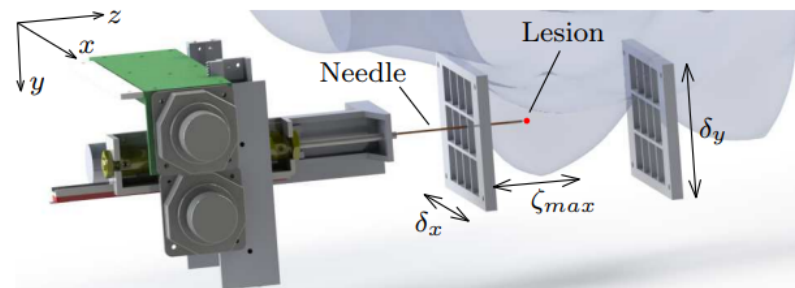


Figure 2.11: Dimensions and prototype of the robotic system by Navarro-Alarcon *et al.*

is transmitted from the actuator to the joint via an aluminium power screw, coupled with a nylon nut. It is a 3 DOF system, actuated with non-magnetic piezo motors and resistive sensors are used for position feedback. It is semi-automatic, with 2 DOF dedicated for aligning the needle guide and 1 for inserting the needle (as shown in fig 2.11).

Park *et al.* [11], using nitinol bendable needle inside a titanium needle guide, designed an automated 4 DOF robotic system (2 DOF for the end effector needle). Figure 2.12 shows the bendable needle and guide (left) and the manipulator (right). The manipulator and end effector are driven by piezoelectric motors, made from non-magnetic materials - bronze, aluminium and its alloys, polycarbonates and plastics, with optical encoders for feedback. The motor controller however were enclosed

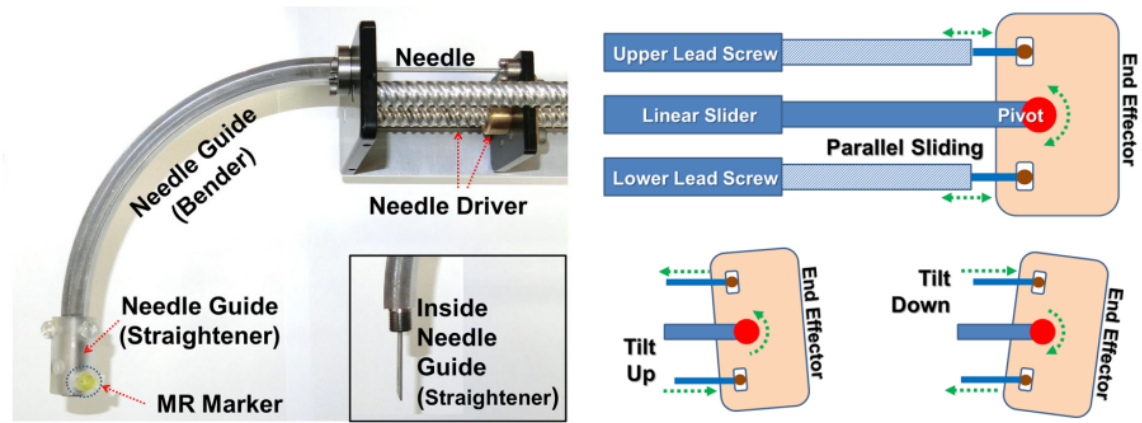


Figure 2.12: Bendable needle structure and manipulator design - Park *et al.* [11]

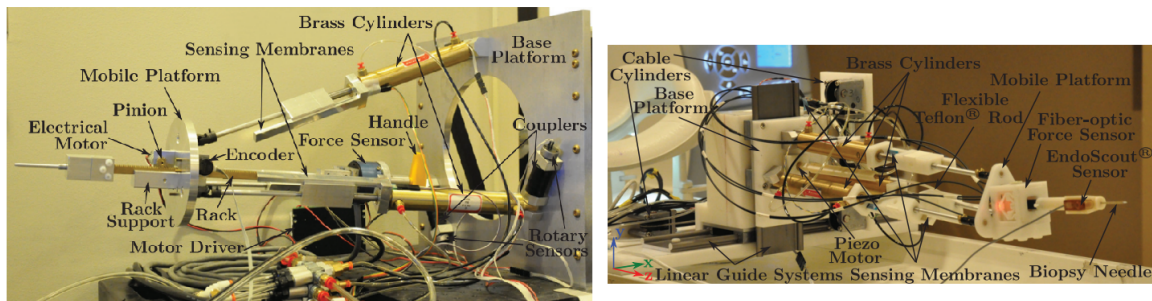


Figure 2.13: Left: Master robot. Right: Slave robot - Yang *et al.* [12]

in shielded aluminium alloy case, with rubber couplings to provide shielding and prevent electromagnetic interference. Yang *et al.* [12] developed a 6 DOF MR compatible master-slave biopsy system, as shown in figure 2.13. The slave robot is constructed with MR compatible actuators and materials such as brass alloy 360, aluminium alloy 3601 for structural parts with high stiffness and hard plastic for other parts, like Delrin®. The four out of the five joints are actuated pneumatically (compressed air) and a piezo motor actuates the last DOF, which is placed outside the scanning center to minimize any interference. The master system has a similar construction as the slave and provides a force-feedback to the user for determining needle insertion positing and feel. Larson *et al.* [13] developed a 4 DOF robotic system to position the device (rotation, compression, vertical probe displacement and probe angle/pitch), one DOF for the probe insertion (as shown in figure 2.14). All the joints are actuated with the help of ultrasonic motors and a combination of telescopic shafts and universal joints help transmit power. The positioning system is completely MR safe and made from MR inert materials.

Groenhuis *et al.* [53] have extensively studied and designed novel pneumatic stepper motors and since have a dedicated research line to developing and design-

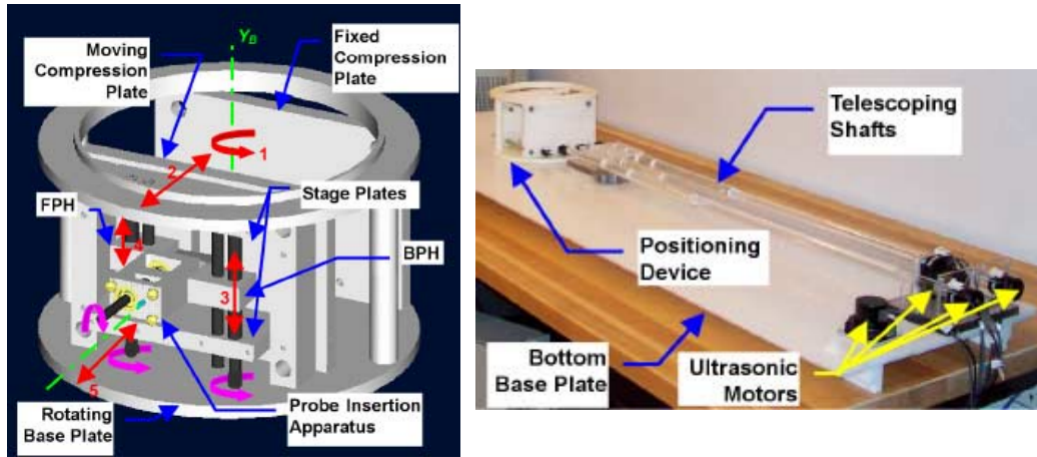


Figure 2.14: Positioning device(left) and a device overview(right) - Larson *et al.* [13]

ing MR-guided breast biopsy systems [45] using those stepper motors. Each system is the next step in development, compared to its predecessor and the pneumatic motors can be laser cut or 3D printed and easily assembled.

Stormram series

The Stormram series started in 2015 [54], with the Stormram 1 (figure 2.15, right). It was the first design of a 7 DOF breast biopsy robot, actuated using seven linear pneumatic motors, each containing a 3-toothed piston. The system resembles a Stewart platform (6 DOF, figure 2.15 left), with a needle insertion DOF on top. With a sequential set of waveforms for each motor, the piston can be made to move the needle in the required motion profile. This displayed the capabilities of the pneumatic stepping actuation but was bulky and large to fit inside the MR bore, along with the patient.

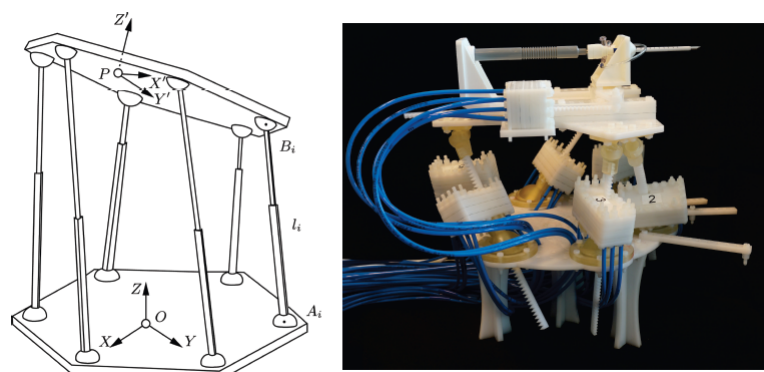


Figure 2.15: Left: Stewart platform. Right: Stormram 1

Stormram 2 was then developed to tackle the two shortcomings in Stormram 1 - large size and lack of computer control. It is a MR safe, five link parallel platform

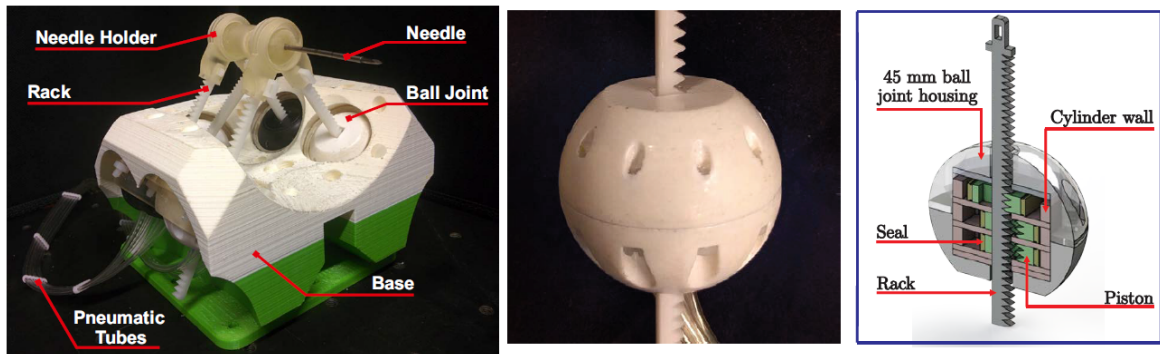


Figure 2.16: Left: Stormram 2. Right: Stepper motor

attached to the base, along with a needle holder fixed on top. Each joint in the needle holder is connected to the frame via a ball joint. Linear stepper motors (figure 2.16, right) control the distance between the joints, thereby actuating the needle holder in the required direction. Like its predecessor, Stormram 2's stepper motors also had three piston, who's sequence of actuation determines the direction and magnitude of displacement. It was smaller than Stormram 1, as smaller stepper motors were designed to fit the 45mm ball joint used in Stormram 2. Experimental studies indicated a targeting accuracy of 6mm in a breast phantom [55]. But the motor forces were not sufficient to precisely insert the needle, specially in dense tissues and the coarse step size, along with the clearances of the ball joints, led to the significant error.

Similar to its forerunner, the Stormram 3 is a 5-link parallel manipulator consisting of 5 linear pneumatic stepper motors to actuate all the prismatic joints. Four out of the five stepper motors have a similar operational design compared to the ones used in Stormram 2 but have a reduced step size of 33% to compensate for the coarser step size and the geometry of the motor housing is redesigned to a cylinder with pin holes, compared to a 45mm sphere to eliminate the excessive clearance issue in the previous design. The fifth stepper motor is the T-49 linear pneumatic stepper motor [56] (shown in fig 2.17, right), which is responsible for the to-and-fro linear motion of the needle. This stepper motor has a theoretical force 2.5 times greater than the other stepper motors used. This is mainly due to the fact that the rack used within the motors are double-sided and the motor is fully 3D printed. Thus resulting in optimised use of space and increased cross-sectional area of the bore, thereby increasing the resultant output force. With these advancements from its predecessor, and extensive experimental testing, the Stormram 3 had a better positional accuracy of the order of 2mm with a repeatability lower than 0.5mm [57].

Up until the Stormram 3, all robotic systems were based on the parallel manipulator design. Apart from the advantage of increased structural rigidity and requirement

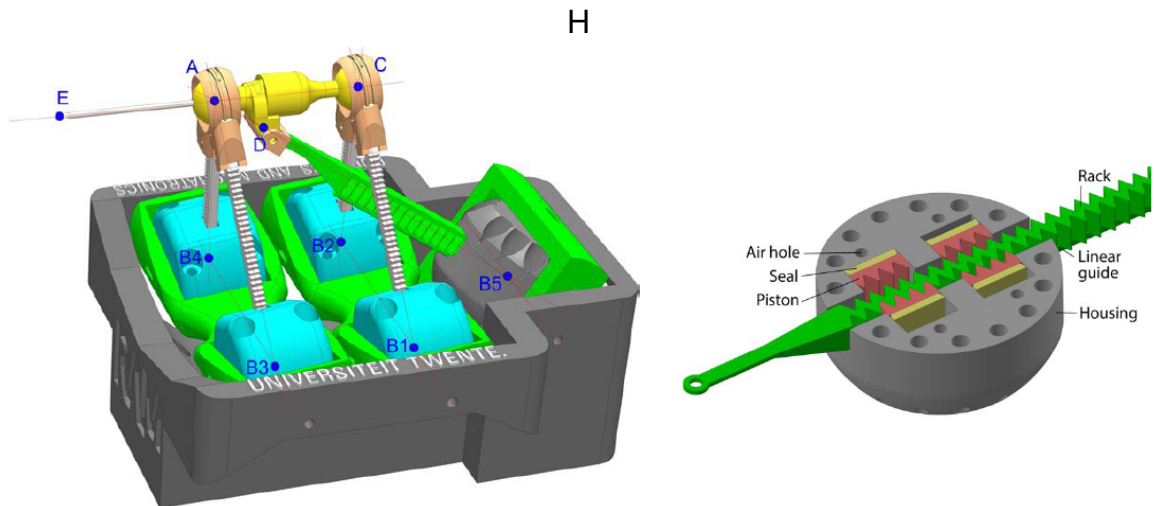


Figure 2.17: Left: Stormram 3. Right: T-49 pneumatic stepper motor

of low inertial forces, parallel manipulators are limited to a much smaller functional work-volume and prone to complex kinematic analyses [58]. This gives rise to the need for a serially linked, open loop manipulator - the Stormram 4.

The Stormram 4 (figure is the first serial link manipulator in the Stormram series, consisting of 4 DOF and actuated by a mix of novel curved and linear pneumatic stepper motors [59]. As open-link serial manipulators are susceptible to vibrations at high operating frequencies and cantilever-like bending due to heavy loads, structural rigidity of such manipulators becomes the main concern that needs to be tackled during the design phase. The stepper motors used in Stormram 4 help eliminate such problems - T-26 linear stepper motor, which is essentially the miniaturized version of the T-49 [56] and a novel C-30 curved stepper motor (as shown in figure 2.18, right). These stepper motors directly actuate the joints, with non-zero hysteresis but zero backlash, as the piston acts as a wedge and fixes the rack in position when the pneumatic pressure is applied.

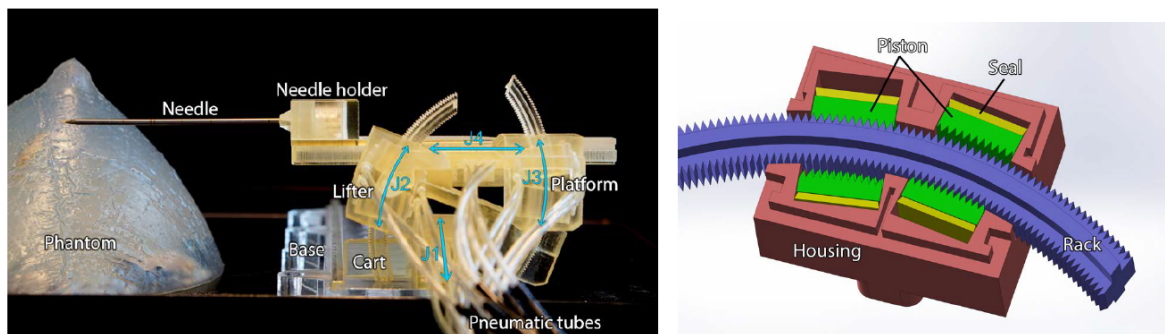


Figure 2.18: Left: Stormram 4. Right: C-30 curved pneumatic stepper motor

Stormram 4 displayed sub-millimeter accuracy, with high precision actuation due to smaller size and lesser number of moving parts. It has an accuracy of $0.73 \pm 0.47\text{mm}$ in free air and $1.3 \pm 0.61\text{mm}$ in the MR environment with a breast phantom.

Sunram 5

Although the Stormram 4 displayed sub-millimeter accuracy, it lacked a few essential features such as a biopsy gun, improved rigidity, safety needle ejection mechanism and a breast fixation system. These limitations are then addressed in the Sunram 5, the 5th generation of MRI-guided breast biopsy robot developed by Groenhuis *et al.* ([45], Chapter 10). The Sunram 5 is actuated using a combination of linear and curved linear pneumatic stepper motors and newly developed dual-speed pneumatic stepper motors [60]. It is a 5 DOF robotic system, which requires 6 pneumatic stepper motors - combination of the first two joint result in a dual speed joint actuation (due to difference in step sizes), and the same thing happens with joint 5 and 6 (as per figure 2.19, left).

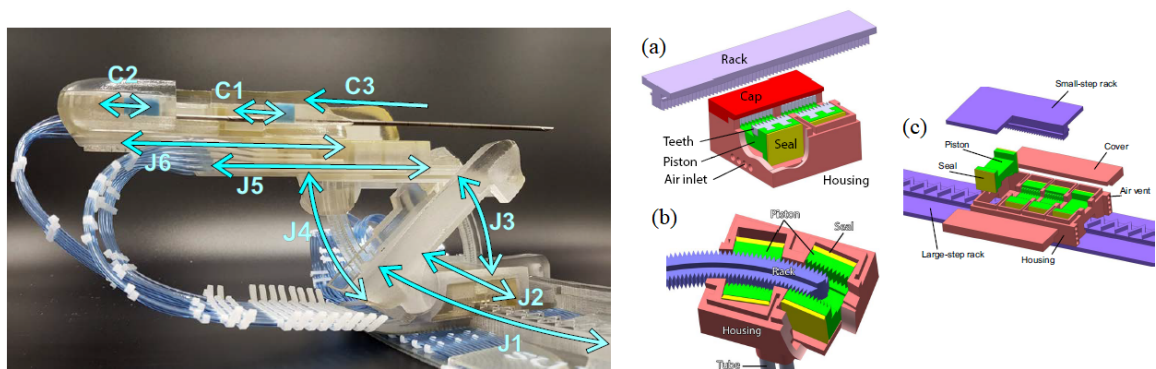


Figure 2.19: Left: Sunram 5 and its joints(J) and cylinders(C). Right: (a)Linear stepper motor,(b)Curved stepper motor,(c)novel dual-speed stepper motor

This design helped reduce actuation time. The biopsy gun is modified to fit into the pneumatic design of the system, with cylinders C1 and C2 firing the needle and performing the biopsy (shown in figure 2.19, left). Cylinder C3 is a single acting cylinder that can be used for ejecting the needle during emergency situations. Along with the Machnet inspired breast fixation system, the Sunram 5 has an accuracy of less than 1mm in free air ([45], Chapter 10). Sunram 7 is the latest robotic system developed and this system is the foundation on which this research is built on. The kinematic and mechanical design are elucidated in Chapter 3.

Sunram 7

Sunram 7 is the 7th generation of research undertaken in the Robotics and Mechatronics (RAM) group at the University of Twente. The research conducted in this study focuses around the Sunram 7's robotic system, developed by Dr. Vincent Groenhuis, and its capabilities to position and control the needle to perform a MRI-guided breast biopsy. Before evaluating the robot's capabilities, first the robot design must be understood and certain aspects, models and functional algorithms must be learnt and designed. This chapter describes the mechanical design and the key components of the Sunram 7, followed by the kinematic modelling done to understand & establish geometrical relations between joints and compute required actuation angles, computation and visualisation of the reachable volume of the needle in 3D space and finally, the interface used to control the Sunram 7.

3.1 Components & Design

Like its predecessor, the Sunram 7 is designed to be a 5 DOF open-link serial manipulator, equipped with a biopsy gun. The system contains a base, four rigid links and an end effector (the biopsy gun/needle). The entire robot, including the actuators, links and other structures are 3D printed using printers from the Ultimaker series. This makes the Sunram 7 a non magnetic, non metallic and non conductive manipulator system. This can be classified as a completely MR-safe device. The only metallic component is the titanium biopsy needle, which can be classified as MR-conditional as it is not magnetic, but metallic and conductive.

The robot is actuated using five rotary pneumatic stepper motors for needle placement, and two cylinders for the needle to perform biopsies and extract tissue samples. The rotary stepper motors are newly designed by Groenhuis *et al.*, which contain two double-acting cylinders acting on a drive gear, and another gear (driven gear) on the same shaft actuates the curved (for rotary joints) and linear (needle

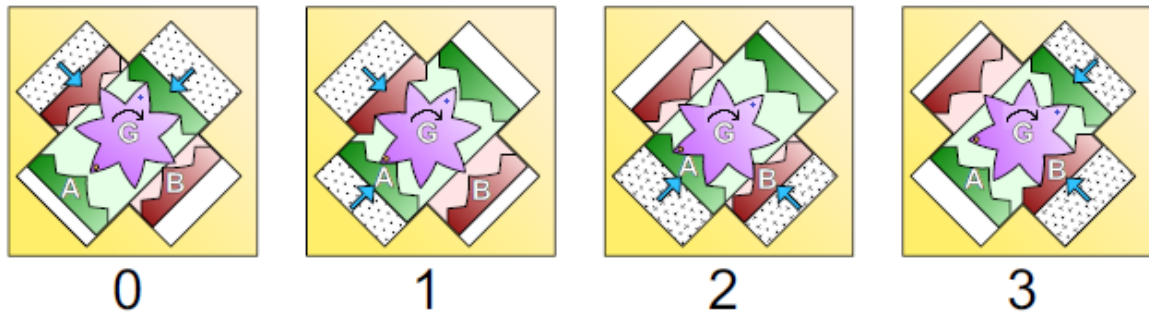


Figure 3.1: Stages of cylinder(A,B) actuation for one-tooth-displacement of the gear(G)

insertion) racks to displace different joints and actuate the robot. As shown in figure 3.1, the two cylinders (A-green, B-red) are placed in a 'cross-configuration' about the drive gear (G-purple). All gears and racks have a modulus of 1 and the driven gear for all motors have 10 teeth. Sequential actuation states of the cylinders/pistons decide the direction of the gear rotation, and frequency of actuation is responsible for the rotational velocity of the gear. Figure 3.1 shows how the gear G would get rotated by one tooth, in the clockwise direction, after 4 stages of pneumatically actuating the pistons A and B in succession.

Figure 3.2 and 3.3 shows the 3D CAD design of the Sunram 7, both at zero position (home pose) and at its extreme position (maximum pose allowed by joint actuations) . It also displays the toothed base (yellow grid-board with the rack) to which the first joint is attached to, the subsequent links and joints, and the robot coordinate frame ψ_B . Joint 1 to 4 all have curved racks, with different radius of curvatures - 264mm for joint 1, 90mm for joint 2 and 60mm for joint 3&4. Compared to Sunram 5, the Sunram 7's first two curved-rack joints pave wave for finer angular adjustments and control, with more freedom in determining the insertion angle. Joints 3 and 4 are responsible for the vertical displacement of the end-effector (similar to Sunram 5), whereas the first two joints are for the horizontal displacements. Joint 5 provides linear motion for the needle holder platform which is in-charge of needle insertion. Table 3.1 summaries the joint specifications, also highlighting the minimum possible step size that can be achieved by the respective joint's stepper motor. First we calculate the effective step size of the piston-gear assembly in the stepper motor based on the gear ratio of the driven gear and the drive gear, which the pistons actuate :

$$\text{effective_step_size} = \pi \cdot \frac{\text{number_of_teeth}_{\text{driven}}}{\text{number_of_teeth}_{\text{drive}}} \cdot \frac{1}{\text{number_of_piston_states}} \quad (3.1)$$

Using the effective_step_size from equation 3.1, we can not obtain the minimum

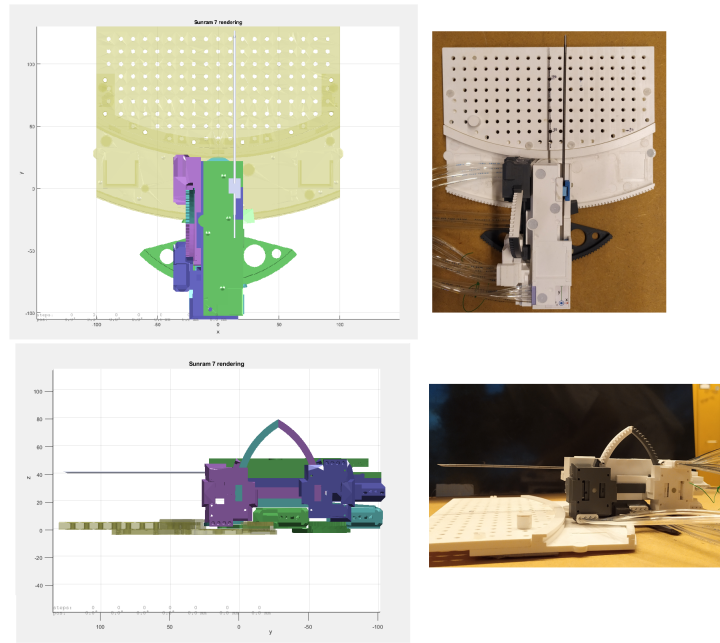


Figure 3.2: Sunram 7 CAD and real robot at zero (home) position

Table 3.1: Sunram 7 joint specifications

Joint	Type	Radius of curvature (in mm)	no. of teeth (drive gear)	Minimum step size	Maximum range
1	Revolute	264	13	0.1311°	-18° to +18°
2	Revolute	90	17	0.294°	-38° to +38°
3	Revolute	60	17	0.441°	0° to 57°
4	Revolute	60	17	0.441°	0° to 57°
5	Prismatic	-	17	0.462mm	-80mm to +19mm

step size of the respective joints, as follows :

$$\text{min_step_size} = \frac{180}{\pi} \cdot \frac{\text{effective_step_size}}{\text{radius_of_curvature}_{\text{rack}}} \quad (3.2)$$

So, for joint 1, the effective step size would be $\pi \cdot \frac{10}{13} \cdot \frac{1}{14} = 0.6041$ mm and therefore, the minimum step size would then be $\frac{180}{\pi} \cdot \frac{0.6041}{264} = 0.1311^\circ$. This is a crucial step which provides the base while converting the required joint actuation angle to the number of steps the stepper motor must execute.

The base and biopsy gun of Sunram 7 consists of many fiducial markers, such as retro-reflective markers, divots for pointer tools, QR codes and MR visible fiducials. As the study revolves around MR-guided breast biopsies, MR-visible fiducials were chosen to be used for any registration or localization tasks. There are 8 such markers on the base - which are essentially cylindrical cavities of same height (3mm)

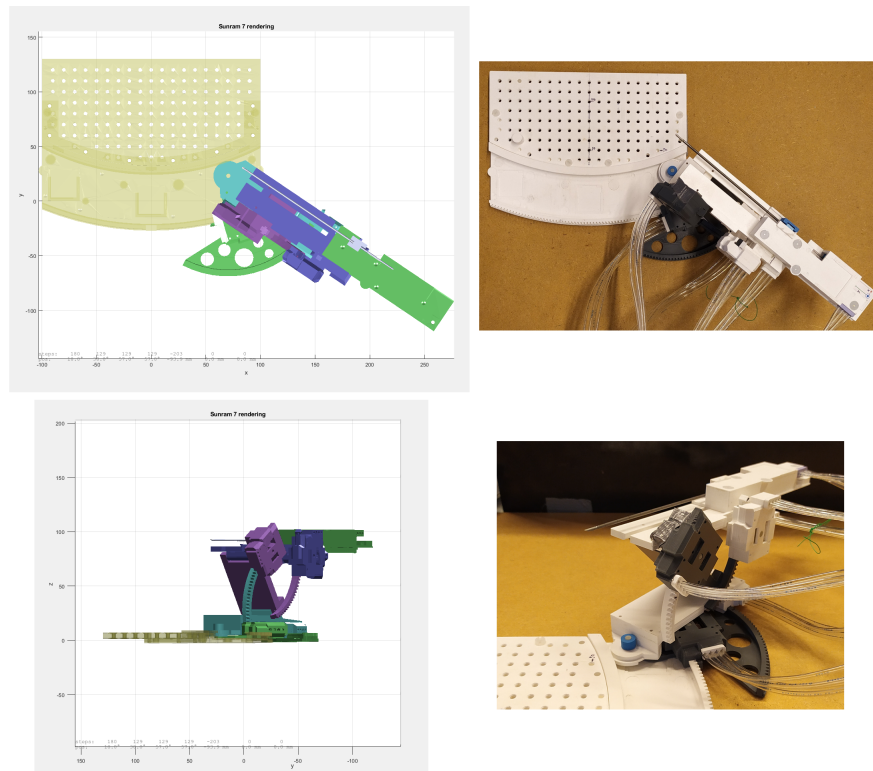


Figure 3.3: Sunram 7 CAD and real robot at the maximum allowed position

but varying diameters (for easy identification), filled with petroleum jelly (Vaseline, as it gives a bright MR signal, when scanned with a specific sequence [61]). The 8 fiducial markers in the base are shown in figure 3.4. Similarly, the biopsy gun is equipped with four such MR-visible fiducial markers, filled with petroleum jelly which can be identified in the MRI scanning sequences to obtain the robot configuration in the MR environment.

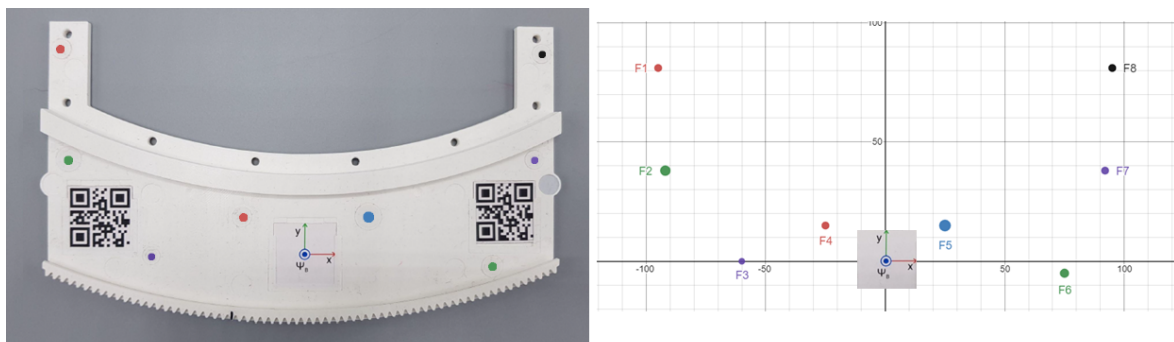


Figure 3.4: The 8 different fiducial markers in the Sunram 7 base frame (F1 - F8)

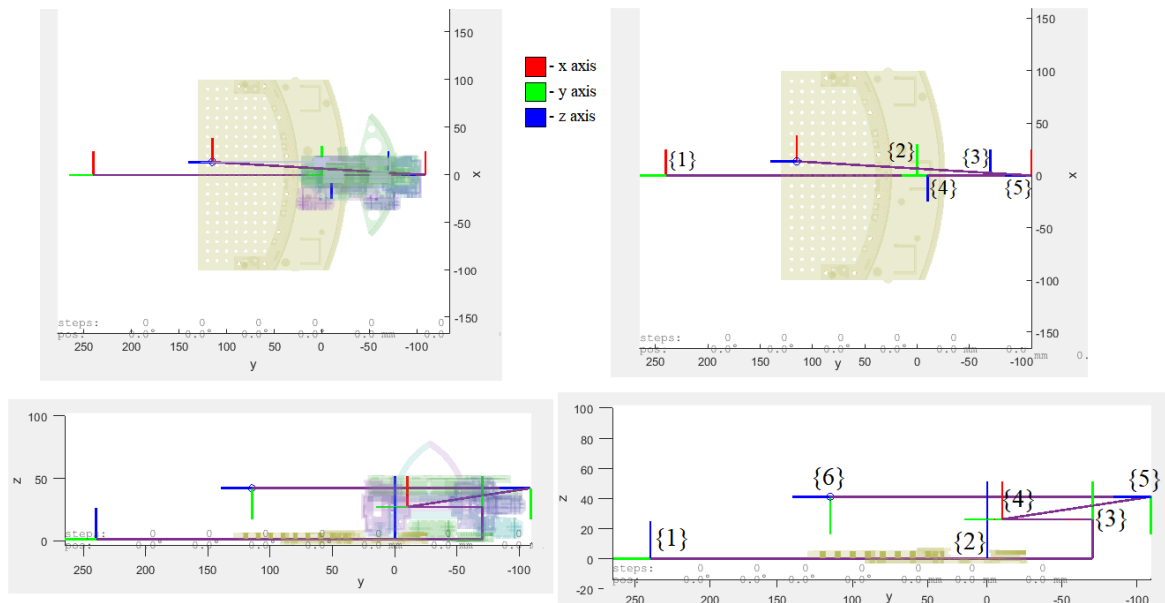


Figure 3.5: Sunram-7 CAD, with the frames assigned as per D-H convention (from frame {1} for joint 1 to frame {6} for the needle-tip)

3.2 Kinematic Model

The kinematic modelling involves establishing kinematic equations which relate the joint space with the coordinate space, to get the orientation and position of the end effector in the frame of reference. This task is divided into two parts - Forward & Inverse Kinematics. The forward kinematic refers to obtaining the end-effector's final position, given a set of joint parameters. The forward kinematic model takes in the joint values and calculates the pose of the serial chain. Inverse kinematics then refers to the opposite - given the desired final end effector position and orientation, inverse kinematic model computes the required joint configurations [51].

3.2.1 Forward Kinematics

A common practice in obtaining the kinematic relations is assigning frames to the joints, in a systematic manner using the Denavit-Hartenberg, or D-H, convention and obtaining the required link and joint parameters [62]. Following the D-H convention, the frames (frame {1} to frame {6}, 6th being the needle tip frame) are assigned to the Sunram 7 system, as shown in figure 3.5.

The joint parameters are the actuation variable for that corresponding joint (angular displacement for revolute joints, linear displacement for prismatic joints), link parameters tell us the relative configuration of one link of the serial manipulator, with respect to the previous link. Using these variables, a transformation matrix can be

Table 3.2: D-H parameters of Sunram 7

Link	α_{i-1}	a_{i-1}	θ_i	d_i
1	0	0	$-90^\circ + \theta_1$	0
2	0	228	θ_2	26
3	-90°	70	$180^\circ + \theta_3$	0
4	180°	60	$-90^\circ + \theta_4$	0
5	-90°	15	90°	$-99 + d_5$
6	0	13.5	0	224

obtained [63], which is defined as :

$$T_i^{i-1} = \begin{bmatrix} \cos\theta_i & -\sin\theta_i & 0 & a_{i-1} \\ \sin\theta_i \cdot \cos\alpha_{i-1} & \cos\theta_i \cdot \cos\alpha_{i-1} & -\sin\alpha_{i-1} & -\sin\alpha_{i-1} \cdot d_i \\ \sin\theta_i \cdot \sin\alpha_{i-1} & \cos\theta_i \cdot \sin\alpha_{i-1} & \cos\alpha_{i-1} & \cos\alpha_{i-1} \cdot d_i \\ 0 & 0 & 0 & 1 \end{bmatrix} \quad (3.3)$$

where a_{i-1} is the link length, α_{i-1} is the link twist, θ_i is the joint angle (variable, if a revolute joint) and d_i is the link offset (variable, if joint is prismatic) and the 4x4 homogeneous transformation matrix T_i^{i-1} gives us the transformation of link i with respect to the previous link $i - 1$.

The transformation from the base frame ψ_B to the end effector frame ψ_E is then calculated by sequentially multiplying the transformation matrices obtained, from the base to the needle tip, as shown below :

$$T_N^B = T_0^B \cdot T_1^0 \cdot T_2^1 \cdot T_3^2 \cdot T_4^3 \cdot T_5^4 \cdot T_N^5 \quad (3.4)$$

where, T_N^B denotes the transformation from (B)ase to the (N)eedle tip.

The D-H parameters for the Sunram 7 were computed and are displayed in table 3.2. Substituting these into the homogeneous transformation matrix in equation 3.3, we get 6 4x4 transformation matrices. The final transformation from base to the needle tip can then be calculated by substituting the 6 matrices in equation 3.4. The final 4x4 homogeneous transformation matrix is simplified and attached in the appendix section A.4. This matrix then provides us with the end effector position, when given the joint configurations.

3.2.2 Inverse Kinematics

In any automated operation, the end effector position is usually known as the motion planning is done with respect to the task in hand. For the Sunram 7, the targets would be the lesions to biopsy. Thus the inverse kinematics would then provide

the joint configurations needed to reach the target position, even in the desired orientation. But this is not as straightforward as the forward kinematic problem. Inverse kinematics are computationally more expensive and non-linearity adds to the complexity. And that is why there are multiple approaches to obtaining the inverse kinematics solutions - algebraic, geometric or numerical solutions [64].

Here, the algebraic solutions are obtained by solving a set of 5 simultaneous equations. These 5 equations solve for 5 variables which define the needle tip position and orientation in the coordinate space - joint angles for joint 1 to 4 and the insertion depth for joint 5. The inputs to this solver would be three target position variables (x, y, z) and two rotational variables (elevation angle - about x_{ψ_B} and insertion angle - about z_{ψ_B}). Three of the five equations are obtained from final transformation matrix (given in appendix A.4) - the first three equations in the last column of the matrix, which pertains to the displacement vector in 3D space. The other two equations are pertaining to the insertion and elevation angles. The equations are as follows :

$$\theta_1 + \theta_2 = \theta_z (\text{insertion angle, about z-axis}) \quad (3.5)$$

$$\theta_3 + \theta_4 = \theta_x (\text{elevation angle, about x-axis}) \quad (3.6)$$

$$T_N^B[1, 4] = X_{target} \quad (3.7)$$

$$T_N^B[2, 4] = Y_{target} \quad (3.8)$$

$$T_N^B[3, 4] = Z_{target} \quad (3.9)$$

where θ_z is the chosen insertion angle, about z-axis, θ_x is the chosen elevation angle, about x-axis, and $T_N^B[i, j]$ refers to the equation at the i^{th} row and j^{th} column of the homogeneous transformation matrix. And thus, solving these equations return the Sunram 7 configuration, i.e. the actuation value for all joints.

3.3 Work Volume

The work volume of a robotic system is defined as the three dimensional envelope that the robot can reach and manipulate. It is the result of the types of joints, their range of motions and the physical dimensions of the links [65]. The workspace or work volume is an important factor to study while determining the functionality of the

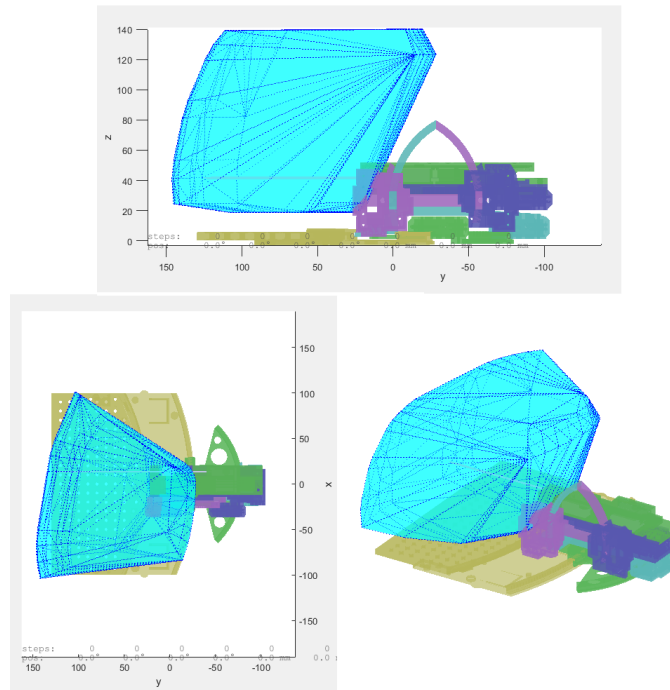


Figure 3.6: The 3D reachable workspace of the Sunram 7

robot as this directly implies physical boundaries within which the robot can perform its tasks - in this case, Sunram 7 performing the biopsy. Given the mechanical design (in section 3.1) and the range of joint actuations, the reachable workspace of the Sunram 7 was obtained and is shown in figure 3.6. This defines the area within which the Sunram 7 can position the biopsy gun/needle tip.

3.4 Interface

The pneumatic motors used to actuate the joints of Sunram 7 consists of 2 double acting cylinders. Each cylinder is then actuated by alternatively pressurizing and depressurizing the two sides of the piston. This is controlled by a 5/2 direction control valves from Festo [66]. These valves have 5 ports, which support 2 directions of flow based on the solenoid actuation of the poppets inside and a spring loaded return system. These valves can help operate the pneumatic stepper motors at high frequencies (upto 100 Hz) due to their fast toggle speeds. Figure shows how one valve controls the cylinders to and fro motion. And so, each stepper motor is controlled by 2 such valves. Each motor also requires 4 pneumatic tube to transport compressed air from the valves to the cylinders. Thus, to actuate the Sunram 7, we need 12 valves, 10 valves for 5 joints and 2 valves for the biopsy gun (one to push the needle inside, other to slider over and obtain the sample) and 24 pneumatic tubes. These tubes are 5-6m long as the entire valve manifold (as shown in figure) is not

MR safe and thus is kept outside the MR scanning room. The valves are toggled with digital signals from an Arduino UNO micro-controller. As the valves require 24V DC to operate, and the arduino UNO only provides an output of 5 volts, a power bridging circuit was designed and fabricated using TIP120 darlington transistors [67] to regulate the electrical power and control the valves. The circuit layout is shown in appendix A.5. With this, the valves can be controlled in any desired sequence to achieve a particular motion profile of the Sunram 7. With the kinematics and interface setup, the Sunram 7 can now be controlled digitally and the subsequent analysis will be carried, with these frameworks in place. The entire Sunram 7 system is shown in figure A.6 in the appendix. For some tests in the MR environment, an extensive controller, designed by Dr. Vincent Groenhuis, is used to control the Sunram 7 - this includes joystick control for each joint, LCD display which displays the step count of each joint and the stepping frequency and the pneumatic valves, along with a pressure regulator (figure A.5

Method & Experiments

This chapter extensively explains the undertaken research methodology, implementation of various software & tools and the subsequent experiments that were designed to be carried out in this study. The first two sections focus on the MRI modality and explains the different approaches taken to segment and isolate the lesions, followed by the registration of the robot in the MR coordinate frame. The subsequent sections then highlight the experimental study conducted with the Sunram 7 to evaluate its performance and accuracy, in line with the scope of the research questions(1.4).

4.1 Research Methodology

The predominant focus of this research is to evaluate the Sunram 7 on its positioning and targeting accuracy, in free air and in the MR environment. So an applied analytical research method is followed [68], where in the theoretical framework and foundations are established using past literature and studies conducted in this domain, and experiments were designed in order to analyse and validate the system performance. At each step, a requirement was stated and the outcome of the applied methods was studied. As Sunram 7 aims to perform MR-guided breast biopsy and help counter the current limitation(section 1.2 & 1.3) in the standard biopsy workflow, a comparative study will also be undertaken to highlight the difference between the manual workflow versus the robot workflow, in terms of the procedure time. The data obtained are analysed in a qualitative fashion, where the experimental results are iteratively obtained to provide statistically significant results. With such an approach followed, this research will then provide a robust conclusions and scope of future discussions in the field of robotic systems for MR-guided breast biopsy.

4.2 Segmentation & Localization

While establishing the forward and inverse kinematic models of the Sunram 7 (described in section 3.2), simultaneous work is carried out to inspect the MRI modality with respect to the acquired scans of the Sunram 7 and the breast phantoms created for this research. Segmentation is defined as the description of structures and areas of interest in the imaging sequence in terms of pixels or voxels, which can be used for identification, labelling and study the components distinctively [69]. Localisation then refers to identifying 'where' the area of interest is, with respect to a particular reference frame.

4.2.1 Breast phantoms

To evaluate the performance of Sunram 7 in the MR environment, breast phantoms were fabricated to emulate a close-to-real breast biopsy scenario. A total of 3 phantoms were used - to study and choose between different MR scanning sequences and to perform needle insertion experiments. The breasts follow a similar material composition of plasticizer. The first stiff breast phantom is made of 100%(600g) of PVC Plastisol (Plastileurre, in French) and embedded within are two fish-oil capsules to simulate lesions within the breasts. Fish oil capsules were used as they give off a bright MRI signal and are cost effective [70]. The second breast phantom is a soft plastisol phantom created, composed of polyvinyl chloride. To emulate and clearly identify the lesions, stiffer dye/ink stained PVC plastisol are placed randomly inside the phantom during the curing process. The third phantom has a stiffness factor in between the first two. It is also made from a similar composition of plastisol and there are many ink-dyed blue and green stiff PVC lesions placed inside to mimic lesions in the breast. The third phantom is then replicated, but this time without the lesions. These phantoms help in studying different MR imaging sequences and in providing a base for experiments in the MR-environment. The three different phantoms are shown in appendix section A.1

4.2.2 MRI scanner and scan sequences

The MR breast imaging technique incorporates an MR scanner, in which the subject has to be placed and adjusted to acquire the breast scans. For this study, the Esaote 0.25T [71] open bore MR scanner was used for any MR scan acquisition. This scanner produces traversal, sagittal, coronal and oblique scanned images. In order to choose the optimal scanning sequence for the breast phantoms, lesions, needle and fiducial markers, imaging sequences from literature are carried out. The

sequences were T1 weighted, T2 weighted, SST1 and 3D Hyce. The Esaote has to be calibrated due to its low magnetic field strength, which causes a certain non-uniformity in the scans. Using a 3D calibration grid and algorithm used by Groenhuis *et al.* ([45], chapter 12), a correction function of the 5th order was computed - which takes in the scanned, distorted image and provides the corrected 3D scans. Therefore, any scans that are made using the Esaote 0.25T scanner, are passed through this corrective function to obtain the final, usable position parameters. Metallic needle is known to distort image quality in the MR scans and create an artifact [72]. And so, the breast phantom scans using different imaging sequences are shown in figure A.2. From this preliminary study, it was found that 3D Hyce imaging sequence provided the best trade-off between the lesion, marker and needle detection/artifacts. The other sequences either could not detect the lesions or had a low performance while imaging the fiducial markers on the base frame. Upon deciding the best scanning sequence(3D Hyce), scans are also taken with and without the needle inserted into the phantom - just to compare the scan quality in the presence of the biopsy needle.

4.2.3 Segmentation

After choosing the 3D Hyce imaging sequence as the most suitable scanning sequence, the next step is to segment the phantom, lesions and the fiducial markers. This is a key step in obtaining the target position in 3D space and registration the scans in the robot coordinate frame ψ_B . 3D Slicer software package [73] is used to visualise, render and segment the breast phantom scans. It is a free, open source software package which is extensively used for medical and clinical research. It contains an exhaustive list of modules and extensions which help quickly model and represent any scans needed for the study. The Segmentation module [74] in Slicer can contour and delineate components of interest. Giving the user the freedom to choose, paint and threshold the regions, it operates with 3D voxels instead of 2D pixels. Once the breast, lesions and markers are segmented, they can be reconstructed and viewed in 3D. Along with just visualisation, using the Segment statistics extension, of the Quantification module on the segmentation results, the physical parameters of the structures segmented can be computed - such as volume, centroid of the mass, surface area and so on. The segmentation process was carried out by executing the following steps:

1. Load MRI scan into 3D Slicer software package
2. Adjust the contrast to the required amount that can facilitate segmentation between different structures.

3. Using tools such as thresholding, paint, grow from seeds and islands, create individual segments for each lesion, the phantom and one for all the markers.
4. Use 'Quantification' module and the 'Segment Statistic' extension to calculate the centroid (in RAS coordinates) of the segmented mass, the Ferret diameter and the lablemap volume of the mass (mm^3).

This data is crucial for now locating the position of different structures, namely the breast, the lesions, the markers and the needle and obtaining their physical characteristics.

4.2.4 Localization

Amongst the different anatomical coordinate systems (also known as patient coordinate system) [75] in which the 3D continuous image samples are taken, 3D Slicer works with Right, Anterior, Superior (RAS) coordinate system. So any location in the scanned 3D image would be represented by a 3x1 vector that returns the R,A and S coordinates. And by using the segment statistics method (described in section 4.2.3), the centroid of each lesion and fiducial markers can be obtained in the RAS coordinate frame. The correction function mentioned in section 4.2.2 requires the inputs to be in the Left, Posterior, Superior (LPS) coordinate frame. And so to obtain the corrected location data of the points of interest, the RAS coordinates must first be converted to LPS coordinates and fed to the 5th order correction function. The obtained rectified LPS coordinates can then be converted back to RAS to maintain the uniformity of the scanned and segmented results in the 3D Slicer software.

4.3 Registration & Transformation

Once the target lesions are segmented and localized, the next task is to obtain the target positions in the robot coordinate frame ψ_B . For this, the entire MR scan must then be registered in the robot coordinate frame, which is where the fiducial markers mentioned in section 3.1 and segmented in section 4.2.3 come into play. There arises a need for mapping between the fiducials location in the robot coordinate frame and the marker position in the MR coordinate(RAS) frame. The process of fiducial registration relies on obtaining a rigid transformation which registers/aligns the two locations onto each other, which can then be used to get map other points from one reference frame to another (in this case, the RAS frame to the robot coordinate frame ψ_B). Rigid or euclidean transforms preserve shape, distances and straightness and as this research is aimed towards accuracy study of the Sunram 7

and its comparison to the standard procedure, while highlighting the error sources, three different rigid transformation algorithms are implemented and analyzed.

All fiducial registration and transformation study, like the forward and inverse kinematics modelling, is done using the MATLAB software [76], which offers excellent libraries and computation capabilities. MATLAB 2021b offers two such functions which take in two datasets containing the position vectors of the same points/markers in different coordinate frames, and returns the optimal rigid 4x1 transformation matrix that can help map one frame to another - in other words, these functions estimate the optimal rotation and translation between two set of points in 3D space. These are the 'estimateGeometricTransform3D' and the 'procrustes' functions.

The 'estimateGeometricTransform3D' [77] approximates and outputs a three-dimensional transformation between two input datasets of 3D points by matching and mapping the inliers from one set to another, using the M-estimator sample consensus (MSAC), which is a variant of the random sample consensus (RANSAC) [78]. This function even let's you control the maximum distance a point has to be, from it' projection. The 'procrustes' [79] function focuses on providing the best euclidean transformation which preserves shapes and also minimizes the sum of squared differences between the points. Along with the transformation, it returns the Procrustes distance, which is an indicator of dissimilarity between the mapped points. The third transformation algorithm is essentially a least-squares problem which computes a rotation matrix which efficiently aligns two vectors of the same order - called the Kabsch-Umeyama algorithm [80]. This technically comes down to solving the singular value decomposition of a certain matrix. Following the sequential steps, a MATLAB function was written which takes in two sets of 3D coordinates and returns an optimal rotation matrix, translation matrix and the least root mean square error between the transformation. After comparing the algorithms, the fiducial registration takes place in MATLAB, where the segment statistic results are fed into the script, which contains the x,y,z coordinates of the markers in ψ_B frame, and the 4x4 transformation matrix is obtained. The process of fiducial registration and transformation is evaluated by studying the root mean square offset between the original marker position in the robot frame versus the transformed coordinates from each algorithm. The fiducial localization error (FLE) is defined as the difference in transformed marker coordinates and the actual marker coordinates. Another measure of deviation is the target registration error, which correspond to the difference between actual and transformed target coordinates (The long and short target markers are shown in figure A.7, left.)

4.4 Joint actuation

This section deals with the actuation of the Sunram 7 robot and verification of its joint motions. After the control circuit and manifold are integrated with the Sunram 7 using 6m long pneumatic tubes, the digital control is provided with a script running on the Arduino UNO microcontroller [81]. The 'PneumaticStepper.h' Arduino library developed by Dr. Vincent Groenhuis provides all necessary functions needed to program any allowed motion in the Sunram 7. A MATLAB script is developed, which convert the joint angle into motor steps needed for that corresponding joint.

With the above resources in place, two Arduino scripts are developed to control the Sunram 7. One is to manually control each joint of the Sunram 7, with a serial numeric input which selects the joint to actuate (1 to 5 for joint 1 to joint 5; 6,7,8 are reserved for the biopsy gun) and one potentiometer knob which controls the steps at a pre-set stepping frequency. The second script takes in the steps per joint that needs to be executed along with the stepping frequency, and based on serial input of the joint number, automatically actuates the joint to the required number of steps. This way, the user has control over the sequence of joints actuations but does not have to worry about manually actuating those joints.

The first step in studying the Sunram 7 is to actuate individual joints to a fixed set-point in the joint space (a predetermined joint displacement), and validate the motion profile by monitoring the angular and/or linear displacement of the needle with respect to the initial home position (figure 3.2). Each joint is independently actuated 4 times, to study the repeatability of the joint motion, while keeping all other parameters constant (the pressure of 1.7 bar , operating frequency of 10 Hz). The experimental setup for these tests consists of the Sunram 7, the control circuit connected with the valve-manifold. A steady clamp on a sturdy stand then holds a camera, which takes the pictures of the needle - before and after actuation of the respective joint. The MATLAB script converts the required joint value into motor steps, which is then fed into the Arduino script which automatically actuates the joint, thereby displacing the needle. The angular displacement of the needle is calculated by overlapping two images on each other - one of the needle at the home position and the other in the actuated position. Using image processing toolboxes in MATLAB, the outer boundary of the needle(in both states) is detected and a first order polynomial is fit to obtain straight lines. The actual motion angle is then obtained by finding the angle between the two linear boundary lines. The linear displacement is obtained in a similar fashion, except instead of the needle boundary, a horizontal line is fit at the tip of the needle(in both states) and the distance between the parallel lines are then obtained, which correspond to the joint 5 displacement.

4.5 Needle positioning accuracy - in air

Once the joint actuations are validated, and before moving on to experimenting in the breast phantoms, the Sunram 7 must be evaluated in free air - with respect to its positioning and targeting accuracy. This section explains the experimental design of the positioning tests in free air. Section 4.6 then elaborates the targeting tests.

Multiple 'target pillars' (figure A.7, right) are 3D printed using the Ultimaker S5 [82]. They are cylindrical solid pillars which a conic tip. Each pillar is of varying height, from 40mm to 100mm, but with same diameter and can be mounted on the grid-board which is screwed on to the base with nylon screws. With this design, the position of the pillar tip is well defined with respect to the ψ_B frame as the grid-board has screw holes at 10mm steps in both x and y directions.

One such targeting pillar, with a height of 60mm, is placed in 15 different position on the grid-board - 5 different coordinates in the x-axis (ranging from -60mm to +60mm) and 3 different coordinates in the y-axis (from 50mm to 110mm). The x,y,z coordinates and the desired insertion and elevation angles in the ψ_B frame are then given as input to the inverse kinematic model developed in MATLAB script (mentioned in section 3.2.2, which then computed the Sunram 7 configuration needed to reach the target. Therefore the 60mm pillar at 15 different x,y coordinates is targeted, with 3 insertion angles (0° , 10° and -10°) and 2 elevation angles (0° and 10°) for each location of the pillar. This gives a total of 95 target poses for the Sunram 7 at different locations within its reachable workspace. The accuracy is measured in terms of the error in the x,y,z directions between the actual needle tip position and the target pillar coordinates, in the robot coordinate frame ψ_B . To maintain uniformity, the joint actuation sequence of the Sunram 7 was kept constant for all targeting poses, i.e. joint 5 was actuated first, followed by joint 3 and 4 at the same time and finally joint 1 followed by joint 2, and the pressure and stepping frequency remains unchanged (1.7 bar, at 10 Hz). This sequence was chosen to avoid any potential collisions of the needle with target pillars and collisions between robot links and components.

4.6 Needle targeting accuracy - in air

The final stage of Sunram 7's evaluation in free air comprises of studying the robot's targeting accuracy - how well is the robot able to target a defined position in free air. The experimental setup for these tests consists of a graph sheet is placed at three different planes parallel to the y-axis in the ψ_B frame ($y = 50\text{mm}$, $y=70\text{mm}$ and $y=90\text{mm}$). The graph sheet was firmly attached with each side under tension to avoid any slack or bending of the paper during the needle insertion process. 5 different x-axis coordinates (from -60mm to 60mm) and 3 different z-axis coordinates (50

mm to 90mm) were determined to be the 'pre-defined' locations which the Sunram 7 would target, by puncturing a hole in the graph sheet at the target points.

The process here is similar to that described in the previous section - once the targets are determined, the MATLAB script is fed with the x,y,z coordinates and the joint angles & motor steps are obtained. The steps are then given as an input to the Arduino code, which then actuates the respective joints. One key difference between this process and the one mentioned in the previous section is that the sequence of joint actuations are different, to accommodate the change in experimental setup. Before placing the graph sheet at the required location, the Sunram 7 is first made to actuate joint 5 with 200 negative steps, which displaces it by 92.4mm in the negative y-axis, and then the biopsy needle is put onto the Sunram 7. This is to ensure that the robot always targets the points on the sheet from one direction only, the positive y-axis. After that, joint 3 and 4 are actuated simultaneously, followed by joint 1 and then joint 2. Finally, joint 5 is actuated to perform the needle insertion towards the target on the graph sheet. The joint 5's actuation steps are obviously adjusted to accommodate the negative 200 steps the joint had to undertake at the start of the process.

A total of 45 points are targeted and punctured by the Sunram 7. The accuracy study includes the measurement of the x and z offset between the punctured hole's center and coordinates of the actual target position on the graph sheet.

4.7 Accuracy evaluation - MR environment

Evaluation of the Sunram 7 in the MR environment is divided into two parts - the first utilizes the pre-operative MRI scans of the breast phantom with lesions, which is segmented and the lesion centroid in the RAS coordinate frame is obtained. This is then passed through the correction function to calculate the corrected lesion centroid coordinates. Using the best transformation (in section 4.3, the MR scan volume is registered in the robot coordinate frame and the lesion centroid coordinates are then mapped to points in the ψ_B frame. With the x,y,z location of the lesion and chosen insertion and elevation angles, the inverse kinematics MATLAB script provides the Sunram 7 configuration and motor steps needed to perform the biopsy. The Arduino UNO is fed with the corresponding motor steps and the Sunram 7 is actuated at a frequency of 10 Hz for all joints but the fifth - the needle insertion takes place at 5 Hz, and a constant pneumatic pressure of 1.7 bar. This entire process happens in the lab, but as the targets are achieved through MR scans, it simulates the entire process happening in the MR environment. Just as mentioned in section 4.6, joint 5 is first made to move back negative 200 steps. Then the biopsy needle is put onto the Sunram 7. This ensures there is no collision of the needle with the breast prior

to the biopsy process. Joints 3 and 4 are then actuated, followed by joint 1 and then finally joint 2. Once in place, the joint 5 starts the needle insertion process. Upon reaching the target inside the breast phantom, the biopsy gun is fired - first the needle is pushed in by 19mm, then the outer needle, i.e. the cutting cannula, slides over the needle, cutting off a sample of the phantom/lesion. Then both the inner and outer hollow needle is retracted back, and the joint 5 then removes the needle by actuating in the negative y-axis. The biopsy sample is then taken out from the needle and analyzed. The targeting accuracy of Sunram 7 is evaluated based on the colouring scheme of the biopsy sample obtained - ratio of the coloured versus non-coloured length of the sample.

The second part of the tests in the MR environment involves placing the entire experimental setup, containing the breast phantom with no lesions and the Sunram 7 with the needle, inside the Esaote 0.25T MR scanner and actuating the robot from outside the MR room. One x,y,z target (0,70,70) with two insertion angles (0° and 5°) and three approach angles (0° , 5° and -5°) were determined to be the target poses for the Sunram 7. The procedure is as follows :

1. Firmly fix the Sunram 7 and the grid-board with the breast phantom attached inside the Esaote 0.25T MR scanner. This position will not change throughout the experiment.
2. Remove the needle and position the robot at its home configuration by visually calibrating the robot to be at the zero positions.
3. Take the first pre-operative scan using the 3D-Hycc scanning sequence. While the imaging is in progress, the inverse kinematic model is set to calculate the motor steps required to reach the first target pose. This optimises the procedure time.
4. Once the scan is complete, actuate joint 5 by 200 steps in the negative y axis. Then go in and place the needle onto the Sunram 7's biopsy gun.
5. Close the MR room doors and actuate the joints of the robot in the same sequence as done in the first part of the MR experiments in the lab.
6. Once actuation is complete, take a confirmatory MR scan with the same scanning sequence and parameters as for the first scan. While this is happening, the inverse kinematic model is already computing the motor steps for the next target pose.
7. Steps 2 to 6 are repeated in order till all 5 target poses are achieved

This experiment forms the foundation to compare the Sunram 7's procedure time to that of the current manual MR-guided breast biopsy procedure, by evaluating the time taken to set up the robot inside the MR environment, actuation and biopsy time and of course the scanning time. This evaluation aims to compare the procedure time which, in the manual process, includes scanning time, inserting and taking patient out from the MR scanner bore, biopsy time and confirmatory scan and/or re-insertion time (if any). The total time taken for both processes would not take into account the time taken to prepare the patient, insert intravenous (IV) line and inject contrast material as these processes are procedure independent and would take up the same amount of time.

Experimental Results

This section extensively elaborates on the outputs and results obtained after each experiment, in order to evaluate the Sunram 7 based on its positioning and targeting accuracy in free air and in the MR environment. The evaluation study is documented in different sections which correspond to a particular test, method or experiment conducted.

5.1 Segmentation

Using the 'Segment Editor' module and the functions within, the breast phantom, lesions and the fiducial markers are alienated to individually study their parameters. To evaluate this step of the overall Sunram 7's biopsy process, the error between the actual fiducial marker diameter versus the segmented ferret diameter is observed. Figure 5.1 show's the error of fiducial markers (F1 to F8, as shown in figure 3.4) and 5 other markers (3 tall, 34 mm and 2 short, 10 mm). The mean error was calculated to be 0.129 mm, which is highlighted with the blue line.

This submillimeter error can be attributed to various factors such as the user's experience in accurately segmenting the structures, their knowledge in the software and/or distorted signal from the MR scanning process. But an overall accurate segmentation process was carried out. And with this confidence, the methods for fiducial registration, transformation and eventually, accuracy evaluation in the MR environment can be carried out. The segmented breast phantom, lesions, fiducial markers and the target markers are shown in figure A.3

5.2 Transformation

To register the lesions and markers in the Sunram 7's ψ_B frame, three different transformation algorithms were studied, in order to evaluate and arrive at the most opti-

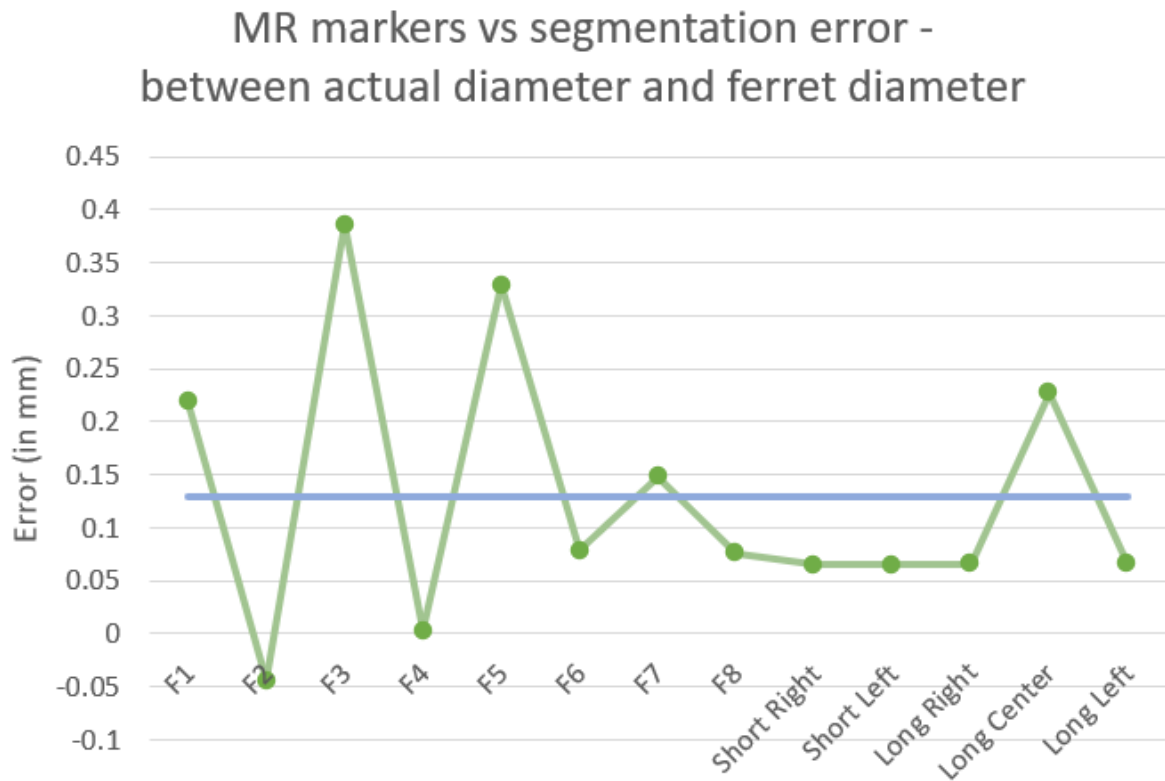


Figure 5.1: Segmentation error for all markers

mal mapping of the RAS coordinates to the x,y,z coordinates of the ψ_B frame. The 'estimateGeometricTransform3D', 'procrustes' and 'Kabsch' algorithms were fed the corrected centroids RAS coordinates of the fiducial marker and the position coordinates in the robot frame. Once each algorithm returned the 'best' transformation, the segmented marker centroids were then transformed to points in the ψ_B frame. Ideally, these transformed points would exactly coincide with the marker coordinates in the ψ_B frame. Figure 5.2 first shows all the fiducial (green) and target markers (blue = long, red = short) in the base frame, the bottom pictures highlights the marker positions in a real experimental setup. To visualize the difference in performance of each algorithm, the actual marker positions and transformed points from each function were simultaneously plotted in the ψ_B frame, as shown in figure 5.3. Where the red points indicate the actual marker coordinates in the ψ_B frame, the blue points are the transformed points obtained from the 'estimateGeometricTransform3D' function, the green indicate the 'procrustes' transformation and finally, the yellow points are the transformation achieved with the 'Kabsch' algorithm. The left image shows the $x-y$ plane, thus enabling visualisation of the deviations in the x and y axis. The image on the left highlights the differences in the z axis.

The fiducial localization root mean square error (FLE) is then calculated in the x,y and z directions. These indicate the deviation of the transformed fiducial mark-

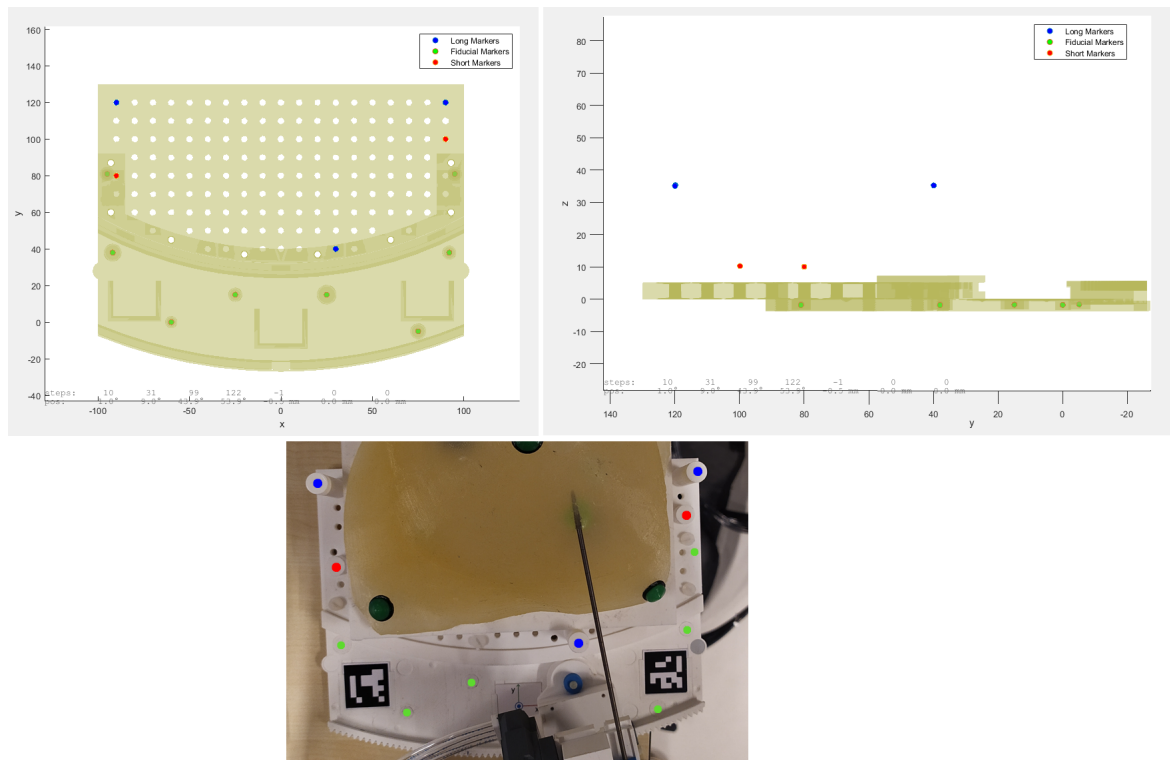


Figure 5.2: All markers on the Sunram 7

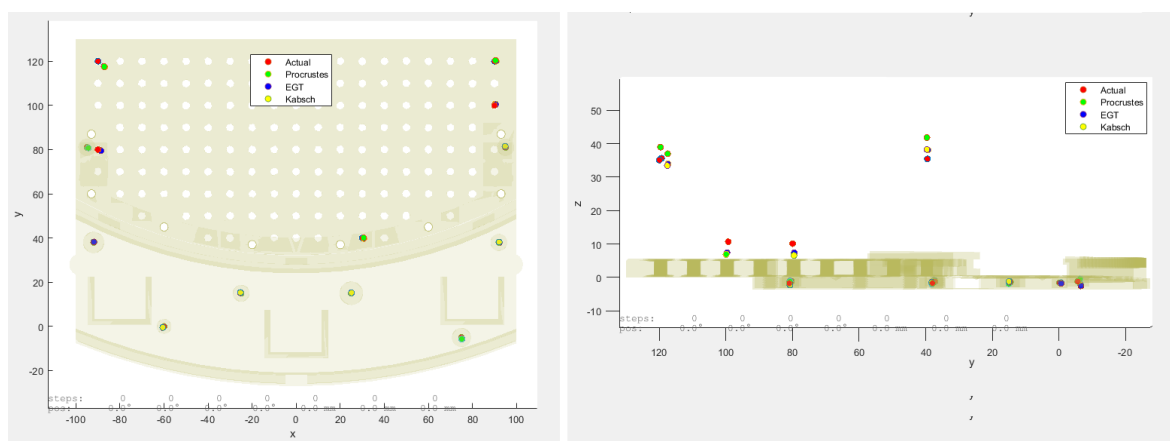
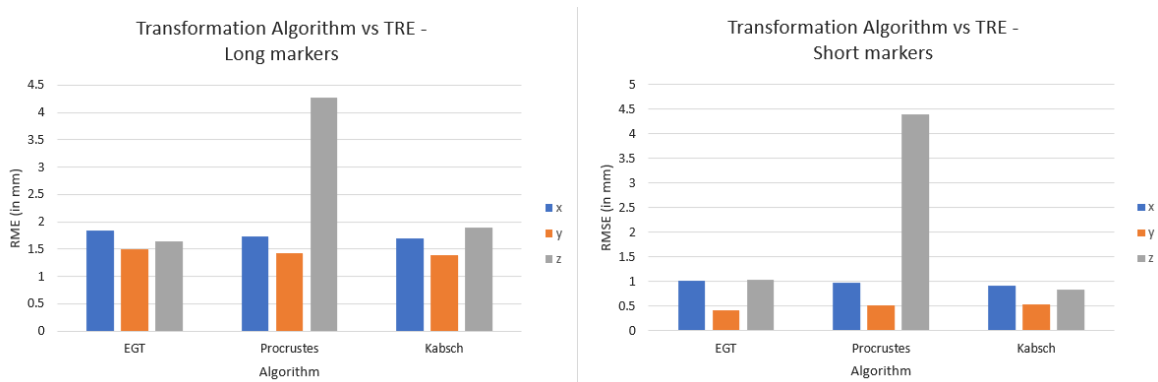


Figure 5.3: Transformation algorithm comparison : actual vs transformed marker positions

Table 5.1: Transformation algorithm vs fiducial localization error, in the robot coordinate frame ψ_B

Algorithm	Fiducial Localization Error (FLE) in mm		
	RMSE_x	RMSE_y	RMSE_z
estimateGeometricTransform	0.3169	0.4245	0.4922
Procrustes	0.3086	0.3918	0.388
Kabsch	0.2994	0.4105	0.3885

ers and the coordinates in the ψ_B frame. Each algorithm successfully returned the respective transformation matrices, with FLE less than 1mm in each axis. Table 5.1 summaries the FLE study results. The second important part of the transformation evaluation is the Target Registration Error (TRE) measure of the algorithms. The three 34mm long and two 10mm short markers act as targets, with their location known in the ψ_B frame. With this, each transformation of the target markers is compared to their known location and the TRE is computed.

**Figure 5.4:** Comparison of transformation algorithms based on the TRE for two targets

The bar chart in figure 5.4 then summaries the TRE results for each algorithm. The chart on the left is for the long markers and the one on the right is for the short ones. At first glance, it is evident that the procrustes function has some bias in the z axis (of about 4mm), but overall, each algorithm performed really well, with almost sub-millimeter accuracy in registering the tall and short targets. The Kabsch algorithm was chosen to be the transformation algorithm due to its overall low and consistent error in each axis.

5.3 Joint actuation

As this research focuses on the thorough evaluation of the Sunram 7 and the potential sources of errors, before testing the needle positioning and targeting accuracy, the actuation accuracy is studied. This process involves setting a constant stepping frequency and pneumatic pressure (10 Hz, 1.7 bar), and while keeping every other joint at a constant position, only actuate the joint being studied with a constant joint value setpoint. Each joint is then evaluated for its repeatability in performing the required motion. The test setup takes pictures from a constant orientation and location with respect to the robot, before and after actuation of the corresponding joint. In this manner, the pair of images can be accurately overlapped on each other and the displacement of the needle can be visualized. This displacement is then calculated with the help of the image processing toolbox in MATLAB, with the methods mentioned in section 4.4. Figure 5.5 shows the different image analysis results for joint 1 to 5. The joints are actuated 4 times each, so to produce a statistically significant repeatability results. The mean absolute actuation errors for each joint as follows :

- $|\text{Joint 1}| = 0.16^\circ$
- $|\text{Joint 2}| = 0.21^\circ$
- $|\text{Joint 3}| = 0.34^\circ$
- $|\text{Joint 4}| = 0.32^\circ$
- $|\text{Joint 5}| = 0.7 \text{ mm}$

These errors can be associated to features such as incorrect or inconsistent calibration of the Sunram 7 (joints not at zero position before actuation), the pneumatic motor skipping steps, and the minute inaccuracies in the image processing procedure due to image quality, environmental lighting and other such noise contributing factors.

5.4 Needle positioning accuracy - in air

The positioning tests described in section 4.5 were carried out for 95 target positions and orientations of the Sunram 7. The positioning error, defined as the difference between the measured position and the true target position, and in this case, the offset of the needle tip in the x,y and z directions from the target pillar coordinates. The results of this study is displayed in figures 5.6,5.7,5.8 and 5.9. Figure 5.6 displays

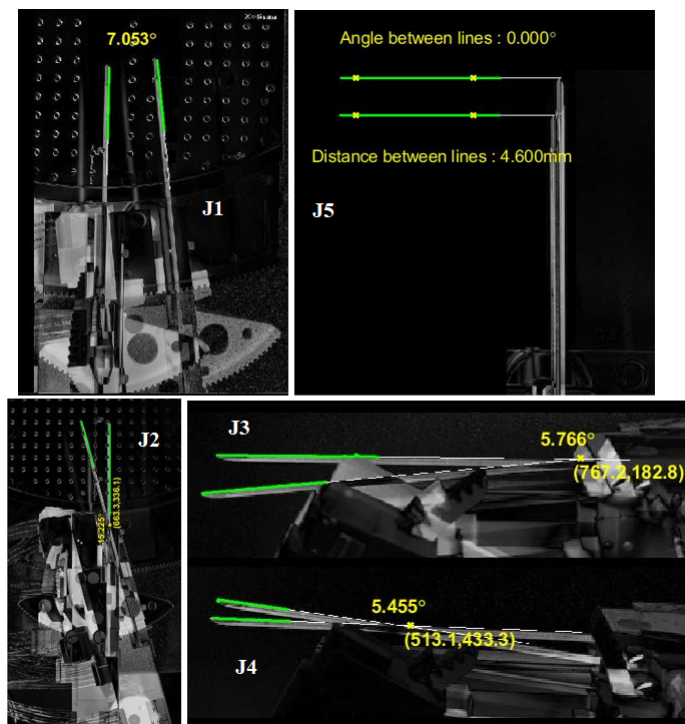


Figure 5.5: Obtained joint actuation displacements with image processing toolbox in MATLAB, for joint 1 (J1) to 5 (J5)

the error distribution in x (blue), y (orange) and z (grey) directions with the spread of target's x-coordinates. It can be seen that the error increase with increase in the target x-coordinate, in either direction. Thus, as the target position gets displayed in either positive or negative x direction, the positional error tends to increase. Similarly, figure 5.7 displays the positional error with respect to target's displacement in the y axis and it's evident that with progression in the positive y direction, the error in each axis increases.

A similar error analysis is then consolidated to study the positional error relationship with the insertion and elevation angles. Figure 5.8 and 5.9 show the positional error distribution and trend with increasing the insertion and elevation angles respectively. One immediate conclusive result was that the least error was the least with zero insertion and elevation angles, with a slight increase with increase in elevation angles and an increase in error in the direction based on the sign of the insertion angles.

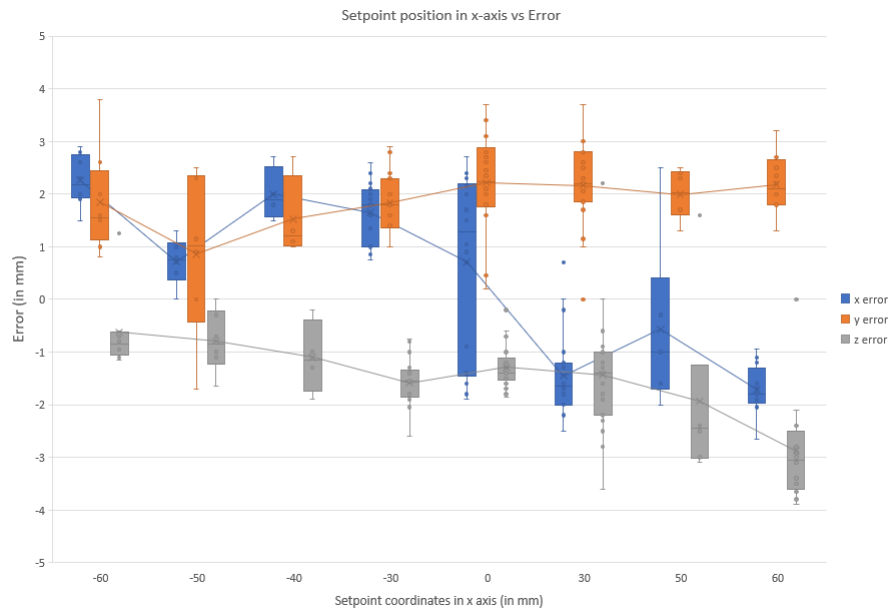


Figure 5.6: Displacement of setpoint position in x axis vs positional error

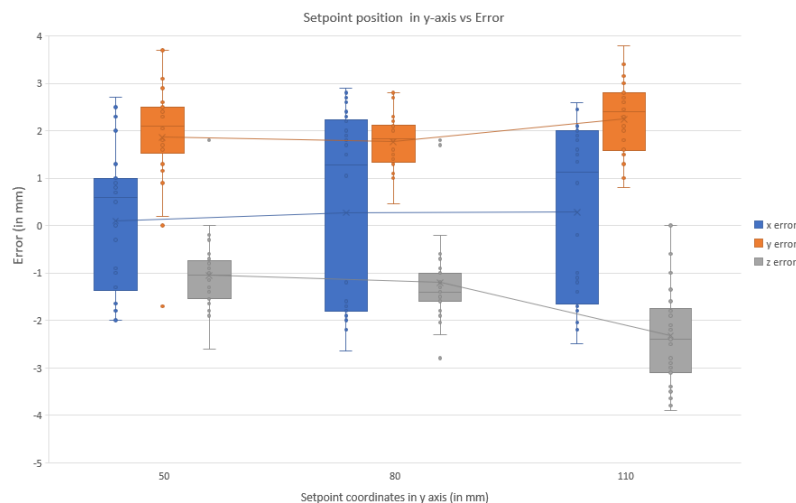


Figure 5.7: Displacement of setpoint position in y axis vs positional error

Multiple observations were made during this experiment. As mentioned, the first was that the error was the least with zero insertion and elevation angles. And as per literature, needle artifact and susceptibility increases with increase in angle between the needle and the scanner's magnetic field. Thus this result proved to be beneficial for the next sets of targeting tests and tests in the MR environment. Second, manufacturing constraints might have added to the error as the target pillars 3D-printed were not their true height, and were always short of their true height by a few millimeters. Third, the dip in error at $x = -50$ mm and $+50$ mm positions in figure 5.6 is a result of fewer tests conducted at those particular coordinates due to the location

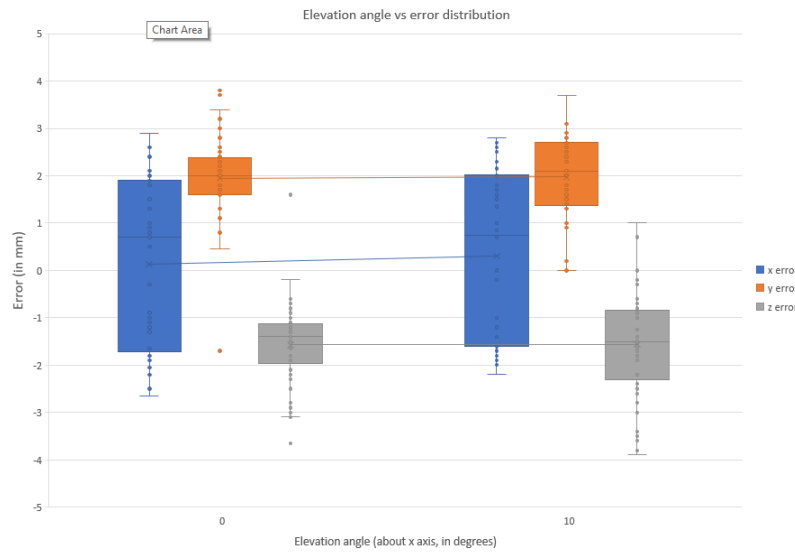


Figure 5.9: Elevation angle about x axis vs positional error

primarily being used for error vs angle tests.

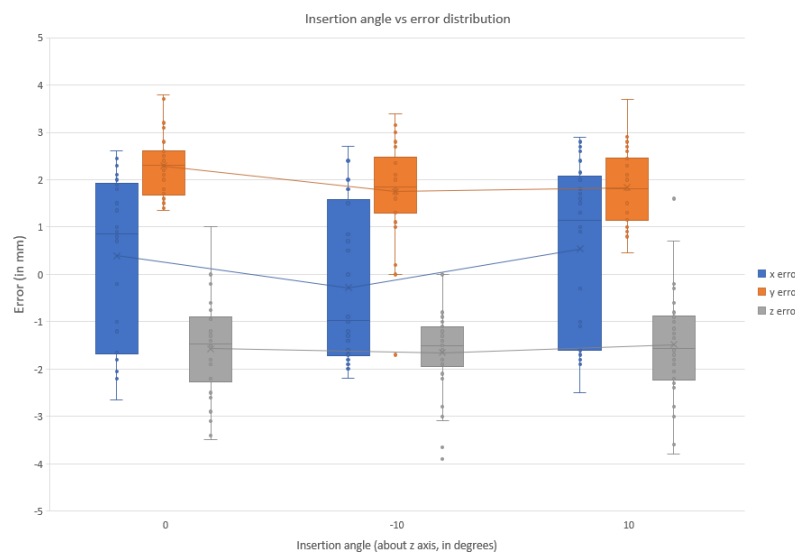


Figure 5.8: Insertion angle about z axis vs positional error

5.5 Needle targeting accuracy - in air

As a part of accuracy evaluations of the the Sunram 7 in air, the targeting accuracy was studied by making Sunram 7 puncture holes on a graph sheet, with targets displaced in x and z directions of the sheet. Same x and z target coordinates were also defined on other such graph sheets, which were then placed at different y locations to obtain the following results, shown in figure 5.10, 5.11 and 5.12.



Figure 5.10: Targeting error along x and z versus target coordinate displacement in x axis

The targeting error is defined as the offset in x and z directions, measured between the center of the punctured hole created by the needle tip of the Sunram 7 and the target's x and z positions on the graph sheet, in the robot coordinate frame ψ_B . Figure 5.10 displays the targeting error distribution with respect to target coordinate displacement in the x-axis. A similar trend is observed, as obtained in section 5.4, wherein the needle tip punctures the target, but with an offset depending on the direction and magnitude of the x axis coordinate.



Figure 5.11: Targeting error along x and z versus target coordinate displacement in y axis

Figure 5.11 and 5.12 highlight similar error distributions, with the mean error slightly increasing with increase in insertion depth (y axis) and target's vertical height (z axis), respectively.

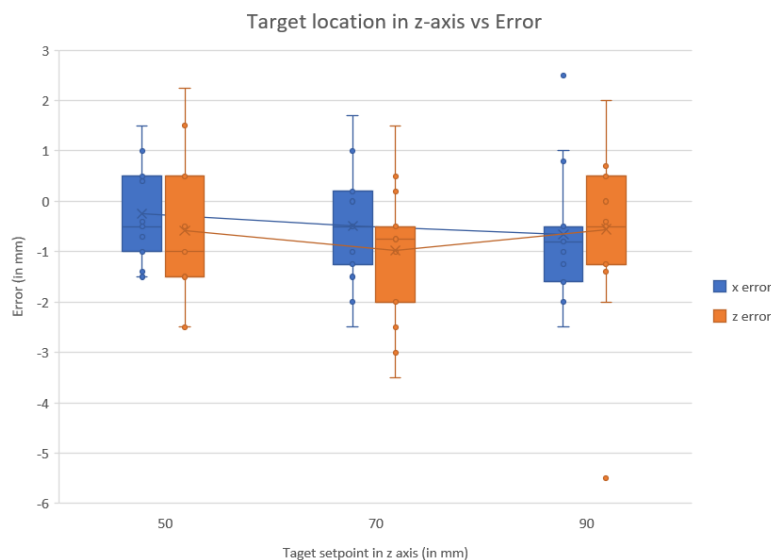


Figure 5.12: Targeting error along x and z versus target coordinate displacement in z axis

Various factors were identified that contribute to these sub-millimeter mean error, between the puncture hole center and the actual target coordinates. With increase in target distance from the ψ_B frame's origin, the error increases which can be a result of missed pneumatic stepper motor steps and vibrations in the needle during insertion process which occur due to manufacturing and design limitations. For any joint actuations close to its maximum allowed actuation range, the heavy 5-6m long pneumatic pipes weighed down the Sunram 7, resulting in resistance in motion while targeting certain setpoints on the graph sheet. The sheet was secured onto the a hollow cuboidal 3D printed structure. under tension on all sided, with one face open to allow the needle insertion in free space without constraining the insertion depth. But there exists some slack which can be noticed at the needle-sheet interface during the insertion process at the target setpoint. The experimental setup and the resultant 'punctured' graph sheets are attached in the appendix section A.7.

5.6 Accuracy evaluation - MR environment

As described in section 4.7, Sunram 7 is a MR-compatible breast biopsy robotic system. And thus, the accuracy and performance studies include an emulation of the breast biopsy procedure in the MRI environment, on a breast mimicking phan-

tom. The setup is labeled and shown in appendix section A.8, and the procedure is extensively described in section 4.7. With this test design, the lesion mimicking coloured stiff plastisol structures were targeted inside the breast phantom and the 'biopsy' results are highlighted in table 5.2.

Table 5.2: Consolidated results from the breast phantom biopsy tests

Biopsy number	Lesion colour	Sample length (in mm)	Coloured segment length (in mm)
1	Blue	8	5.4
2	Blue	5	4.4
3	Blue	6.35	0
4	Blue	8.6	6.1
5	Green ₁	9.8	0
6	Green ₁	9	3.2
7	Green ₁	12.6	2.2
8	Green ₂	8.9	0
9	Green ₂	9.65	4.6
10	Green ₂	7.3	3.1

The biopsy samples obtained are also shown in appendix section A.8. A biopsy is classified to be successful "if the ink-stained portion of the sample is at least 2mm in size" ([45], chapter 15). From table 5.2, it is evident that, as the Sunram 7 has an accuracy within millimeters, the biopsy needle would more or less reach a similar target site within the phantom. And this can be observed with the first four biopsy tests conducted on the 'blue' lesion - keeping the insertion angle and elevation angles the same, the length of the biopsy sample showed a steady decrease, and the coloured sample length also decreased, until a point where no coloured sample was obtained. Then the insertion and elevation angle were chosen at random and the fourth iteration of the biopsy sample of the blue lesion was obtained successfully. A similar trend can be observed with two green lesions, but in this case, the lesion was either missed or the biopsy was not successful as the coloured sample length was close to zero. But then reiterating the process resulted in a green biopsy sample retrieved from the biopsy gun, with decreasing coloured sample lengths. With 10 such biopsy process iterations, the Sunram 7 obtained a 70% successful biopsy rate. The biopsy sample results are shown in the appendix section A.11.

5.7 Comparison with standard biopsy process

This research aims at solving space and time restricted MR guided breast intervention processes. And the final evaluation of the novel MR safe system involves comparing the workflow of the current standard manual breast biopsy process with that used with the Sunram 7, particularly focused on the procedure time and highlighting the advantages of each. For ease of understanding and comparing Sunram 7's biopsy capabilities with current practices, a manual MR guided breast biopsy was observed at the ZGT [83] hospital at Hengelo, The Netherlands, who's workflow is compared in the upcoming section.

A typical biopsy procedure takes about 60 to 90 mins [84]. The procedure observed at the ZGT hospital lasted 53 mins. This does not include the time taken for the pre-operative MRI scans taken much before the procedure but includes time taken for device setup, subject insertion and removal from the scanner's bore, multiple MR scans and the biopsy process itself. The sequential workflow is as follows :

1. Visual inspection of the MR scanner and any adjustments in the bed and coils is done, while the subject is being questioned and prepped.
2. Subject is made to lay down in position on the bed, and the biopsy grid system is firmly placed, to compress the breast and place the calibration marker for transformation and planning.
3. Quick confirmatory scans are taken
4. Multiple MR scans are then taken to locate the lesions or to image a certain region of interest. These scans are subtracted to clearly localize potential biopsy spots.
5. Upon registering the marker and choosing the tissue area to biopsy, the software provides the best insertion location and depth.
6. The subject is taken out from the MR bore, and the radiologist perform the needle insertion using the needle guide and the information provided in the previous step.
7. The subject is taken back into the bore, to confirm the needle position. If in the correct location, the patient is taken out from the bore to perform the vacuum-assisted biopsy process.
8. Once the tissues samples are extracted, a marker is then placed at the biopsy spot for future imaging and diagnosis .

9. Subject is taken out from the MR room, provided with any assistance and reconfirmation they require, the process is complete.

The biopsy process by itself (steps 6 to 8) takes 6-9 minutes, including the needle insertion, post-biopsy confirmation scan, and marker placement. Steps 1 to 3 take approximately 19 minutes. Processes like registration of marker and multiple subtraction scan acquisition (steps 4 and 5) roughly ends up taking 12 minutes. Thus the total procedure time for the manual biopsy is approximately 40 minutes. Keeping this procedure as the standard, the Sunram 7's biopsy process is then compared by individually adding the the total time taken for the biopsy process - from the lesion localization up to the sample tissue extraction. The needle positioning process inside the MR environment gives us the equivalence of the procedure time, added to the time taken for the actual biopsy to take place (as in section 5.6 The workflow for the Sunram 7 is as follows :

1. Obtain pre-operative scans, load them into the 3D Slicer software, and segment out the markers, required lesion structures and regions of interest.
2. Obtain the centroid position of each fiducial marker. Load them into the MATLAB script and obtain the transformation.
3. Using the transformation, obtain target coordinates (obtained in the MR coordinate frame) in robot frame and input that into the Arduino script.
4. The Sunram 7 is placed in position, and the 5th joint is actuated to retract by a set distance.¹
5. Then the needle is fixed in place and the Sunram 7 is actuated in the following order - joint 3 and 4 together, followed by joint 1, then joint 2 and finally, joint 5 inserts the needle.
6. Upon reaching target, a quick confirmatory scan can be obtained.
7. Biopsy is performed by firing the biopsy gun, and the tissue sample is obtained once the needle is retracted.

Steps 1 to 3 happens before the actual MRI biopsy procedure and so, even though a crucial step of the workflow, it does not contribute to the procedure time and is equivalent to the pre-operative scans and procedures carried forth in the current manual biopsy procedure. Steps 4 and 5 comprise of MR scanner and robot setup time, which is a cumulative sum of the time taken to calibrate the robot to its home

¹Sunram is actuated at 10 Hz (joint 5 retraction at 10 Hz, insertion at 5 Hz), with 1.7 bar pressure.

position (without the needle, 2 minutes), time taken to actuate joint 5 by 200 steps in the negative y axis (about 34 secs) and then place the needle back into the robot(2 minutes). Apart from the time taken for the inverse kinematics algorithm to return the joint configuration for the target location(up to a minute), it also includes the robot actuation time for the needle insertion process, i.e. the time taken to actuate joint 3&4 together, then joint 1, then 2 followed by joint 5. This actuation time can vary based on the target location in the ψ_B frame and the stepping frequency of the pneumatic motors, but at 10 Hz, it usually takes a maximum of 5 minutes. Once the needle is inserted, a confirmatory scan is taken (step 6). The 3D Hyce scanning sequence was used, which took roughly around 5 minutes and 30 secs. During this time, the pre-operative scans of the other subjects were analysed and segmented to best optimise the procedure time. Once confirmed that the needle is at the right place, the biopsy is performed and the tissue sample is obtained (step 7). From here, the procedure is equivalent to the current manual procedure where in the patient is comforted while the samples are obtained, and the process is complete. Thus, the total biopsy procedure times for the Sunram 7 is approximated to be around 19 minutes. This does not include the pre-operative scans or the lesion registration processes as this can happen even before the patient shows up, as in the case of the current procedure. Other processes such as preparing the subject, insertion of IV, contrast material and reconfirmation are independent of the procedure and take a fixed amount of time. But as one can notice, the entire process time has been reduced considerably due to the elimination of the requirement to remove the subject outside the MR bore at anytime of the operation, as all operations happen in-situ. The additional time requirement for the radiologist to remove the needle, place a plastic for confirmation, remove it and then biopsy using vacuum assisted device and take another confirmation scan is reduced as the hollow needle biopsy gun by itself acts as an indicator for positioning confirmation, performs the biopsy and retracts to position with the biopsy sample.

5.8 Discussions

This section aims to concisely summarize the evaluation design and criteria implemented to study the Sunram 7 and its breast biopsy capabilities. This was achieved by setting up the prerequisites such as the forward and inverse kinematic model and fabricating the electronic control interface. Segmentation and localization were performed in the 3D Slicer software, with an accuracy of 0.129 mm, as shown in figure A.3. The transformation was obtained by feeding the Kabsch algorithm with marker centroid positions in RAS coordinate system and obtaining the transformation, using which the lesions are then registered in the robot frame. As this study evaluated the

Sunram 7 biopsy process and its accuracy, the errors in each step were identified - inverse kinematics model consists of approximations and round-off errors due to solving 5 simultaneous and/or non-linear equations using MATLAB toolboxes. Segmentation is entirely user dependent, which can be avoided if 3D-visualisation is not of key importance, as long as the marker and lesion centroid (or location of dropped fiducials, in absence of segmentation) are made available for the transformation script in MATLAB. This transformation algorithm also adds on another error layer, pertaining to influence of outliers and over-fitting.

To first evaluate the Sunram 7 robot, each joint was independently actuated and checked for its repeatability, which even though provided reliable results, had some mean offset from its actual required position, adding to yet another layer of error. This error can be associated with the discretization error due to the constraint of the steps needing to be whole numbers, the pneumatic motor skipping steps, and influence of the weight of pneumatic pipes on the manipulator. But this displayed the Sunram 7's accuracy in the joint space. Similar influences of error can be found while studying the positioning and targeting accuracy of Sunram 7 in air and in the MR environment. Even the distance of the target from the robot's origin plays an important role in determining the influence of the robot's own weight on the positioning accuracy. The mean 3D offset between the actual needle position and the targets were found to be 3.183 ± 0.809 mm. The mean positioning errors corresponding to each axis and the mean 3D offset between the measured needle tip position and the actual target is shown in table 5.3.

Table 5.3: Mean positioning error and standard deviation in each axis, and the mean 3-D distance between measured needle tip position and actual target location

	Positioning error (in mm)			Mean 3D offset (mm)
	x	y	z	
Mean	0.298	1.959	-1.558	3.183
Std.Dev	1.692	0.812	0.955	0.809

In a similar fashion, the targeting error is described as the mean offset in 2-D x-z plane at different distances in the y axis, between the measured 'hole center' created by the needle and the actual target coordinates on the graph sheet. A 2-D targeting offset of 1.743 ± 1.039 mm is achieved with the Sunram 7. The results are documented in table 5.4. This concludes the accuracy evaluation of the Sunram 7 in the robot coordinate space and free air.

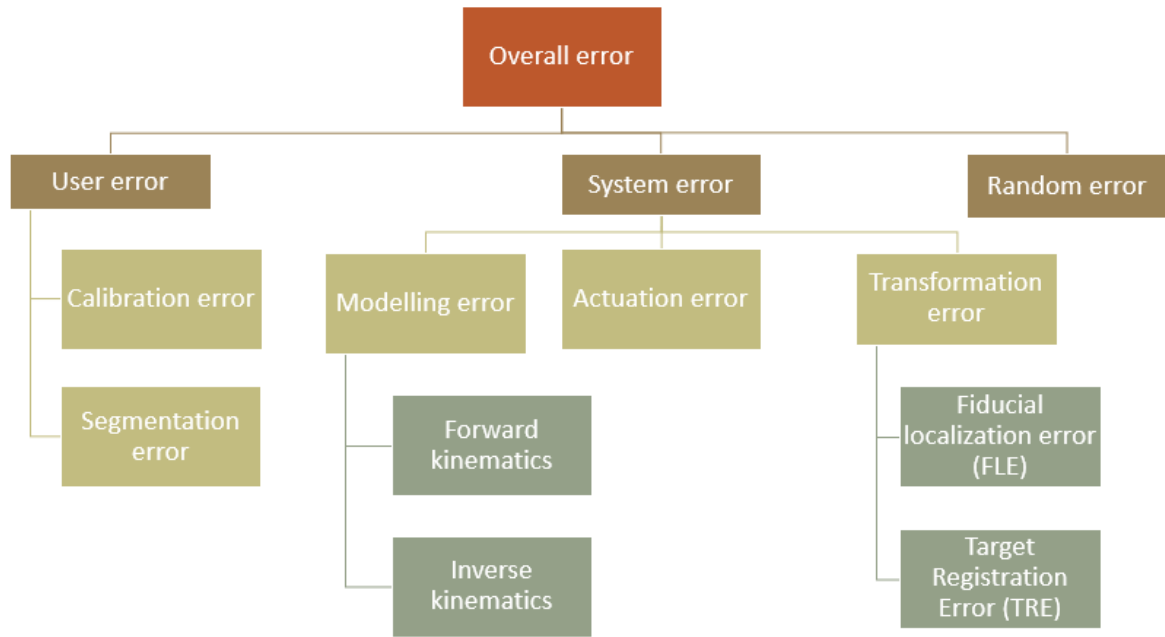


Figure 5.13: Different possible sources of error

Table 5.4: Mean targeting error in x and z axis, with the mean 2-D offset between measured target position and the actual target coordinates

	Targeting error (in mm)		Mean 2D offset (mm)
	x	z	
Mean	-0.462	0.263	1.743
Std.Dev	1.128	1.60	1.039

In the breast phantom, the phantom-needle interaction is not considered within this scope of the study, though it plays a predominant effect on the needle insertion process. Compared to the standard process, the Sunram 7 clearly seems to take lesser biopsy procedure time as it performs all activities inside the bore (around 18-20 minutes). It helps reduce tissue damage as well - as currently, to compensate for the lack in targeting accuracy and the intuitive play by the radiologist, large amounts of tissue samples are taken (8-10 samples [46]). But the Sunram 7 only extracts a long tissue sample (figure A.11), with accuracy in millimeters. There is a reduction in random positional movements as there exists no requirement for the patient to come out of the bore frequently, thus preventing excess tissue removal and biopsy process damage - with a biopsy success rate of 70%. The possible, different error sources were identified and categorized as per figure 5.13

The user error is, as the name suggest, user dependant. As this is a robotic system, which provides a certain degree of automation, the user error exists but is

restricted to calibration of the robot (to its zero or home position), the identification of the region of interest and the segmentation experience. From here, the overall error then is a cumulative effect of system and random errors. System errors starts from the modelling of the Sunram 7 in MATLAB, specifically the forward and inverse kinematics. These are geometric, trigonometric equations which include rounding off and certain approximations. Also, solving a set of non linear equations using MATLAB toolboxes and solvers would induce a certain error due to the efficiency of the algorithms used and of course, the memory constraints of the system. Actuation error corresponds to the effective motion produced by pneumatic stepper motor, used to actuate the Sunram 7. These motors can induce error in the Sunram 7's final configuration by having some offset in the joint actuations due to manufacturing errors in the racks or gears which induce some inaccuracies in the motor functioning, missed steps due to high stepping frequency or low pneumatic pressure. This error can also be induced due to Sunram 7's physical design and layout, wherein the weight of the pneumatic tubes tend to apply some force/tension on the robot, causing it to miss steps. The transformation error is the difference between the fiducial markers location in one frame and the transformed marker points, from the MR frame to the same reference frame. As the algorithm has its own efficiency in finding the optimal rotation and translation, there exists a localization error for the fiducial markers. This thereby gives rise to the target registration error, which is essentially the difference between the actual target location and the transformed target location, from MR frame to the robot reference frame using the optimal transformation achieved during the fiducial registration step. As one can notice in fig 5.4, the Procrustes transformation algorithm displays a bias of 4mm, particularly in the z axis, for both short and long target markers. Due to initial programming logic error, this error was roughly 8 mm. After debugging and validating the script, the source of this systematic error could not be identified, and for this reason, the Kabsch algorithm was chosen for any and all transformations in this study. Any other error can be associated to random biases in the system or the experimental setup, which cause normally distributed variance in the system - some vibrations or resistive forces, imaging modality disparities and so on. Yet, the Sunram 7 has displayed accurate results in this study to achieve the requirement of performing a biopsy in the MRI scanner, within the given tolerance. As the average lesion size ranges from 3 mm to 70 mm [85], the Sunram 7 has shown that it can perform a successful lab setup biopsy accurately, even with the effect of all the errors mentioned above.

Conclusions and recommendations

Apart from the obtained and derived conclusions from the entire Sunram 7's evaluation study, future scope and recommendations are also discussed in this chapter.

6.1 Conclusions

The Sunram 7 is a MR safe, pneumatically actuated, 5 DOF breast biopsy robot, designed and developed by the Sunram team at RAM, to combat the ergonomically operable space constraints within the MR scanner's bore, without affecting the scanning image quality, thereby eliminating the need for the patient to be taken in and out of the scanner. This study focused on how to effectively localise the lesions, for the Sunram 7 to accurately target, after studying the robots positioning and targeting accuracy - both in free air and in the MR environment. While simultaneously deciding between the best transformation algorithm and ensuring that any error is within a set threshold. This threshold is the average lesion size. Lesions can be identified and segmented in the 3D Slicer software with ease, but is user-experience dependent. This software provides enough modules and extensions for the user to design their own application and returns accurate results. As evaluated during the segmentation and localization study, the segmentation error was found to be 0.129 mm, depicting sub-millimeter accuracy. Transformation algorithms were tested out to check which provided the best rotation and translation between the marker positions in the coordinate frames, with respect to the marker choices, design and location in the Sunram 7. Kabsch algorithm worked best, with minimal fiducial localization error in x,y and z axes of the robot coordinate frame ψ_B (0.3 mm, 0.4 mm and 0.4 mm respectively) and low target registration root mean square error of 0.64 mm in 3D space. With these subsystems in place, the lesions can accurately be registered in the robot coordinate frame.

Pneumatic stepper motors provide an excellent actuating option within the MRI

scanner, with it having no impact on the imaging sequence but also providing sufficient force to ensure needle insertion in the breast phantoms and to keep the robot stiff during the actuation or biopsy process. The breast phantom aim at emulating different stiffness breasts and the possible lesions. The drawback of such phantoms are the ability of plastilleure to disintegrate over long times, and under stress if it is too soft. The Sunram 7, being an open link serial manipulator, displays accurate needle placement in free air with an error of $3.2 \pm 0.8\text{mm}$, while also covering a large work-volume to operate within. In the MR environment, the Sunram 7 was able to accurately and successfully biopsy the stiff PVC lesions, 7 out of 10 times, thus displaying potential in its implementation for MR-guided breast biopsy process. With reduced procedure times (approximately 19 minutes) compared to the current manual process (40 minutes), potential for lower tissue damage due to its accuracy and repeatability, the initial proof of concept and evaluation of the Sunram 7 has proven its candidacy to assist with or even perform a full clinical MR-guided breast biopsy.

Before this scientific study finally results in a product for clinical application, much like any medical advancements, a significant amount of development and testing time must be invested. The error sources identified in this study can be compensated for to better the system substantially. Many women would benefit from technology advancements in screening and detection of breast cancer, which is already proven to be a deadly disease. The technology created via this study may not offer an instant benefit in that regard, but it may at least be a step in the right direction.

6.2 Recommendations

This study extensively examined the Sunram 7 aimed towards the breast biopsy process using the MRI modality. Even with accurate results and a successful 'biopsy' rate, integrating such a robotic system in current clinical practices requires several technical and non-technical improvements.

In the technical side, the pneumatic motors might need a stronger sealing system, since the compressed air seemed to progressively leak as the tests were conducted. As mentioned in the discussion section, the pneumatic tubing add a certain directional tension on the Sunram 7, possibly due to it weighing more than the robot itself. These tubings can either be evenly distributed about the Sunram 7 robot or a lighter, different material tubes can be incorporated. The free length of the needle in the biopsy gun will always deform during insertion processes in a phantom, due to the cantilever action between the needle-tissue (phantom) interaction force and the fixed point on the biopsy gun. A quick work-around was designed to add onto the far

tip of the needle holder (as shown in fig A.12, which reduced the free length of the needle and helped reduce the needle bending. This also latches off if the insertion process involves the needle holder to move past the fixation point of this 'needle guide'. Having said this, a better solution might have to be worked around to address this bending moment. The other development domains to focus on are in the field of quick and better calibrations methods, real-time position sensing inside the MRI scanner and integration into a breast coil. Lastly, experiments with the Sunram 7 could be undertaken in a real setting, i.e. under the same conditions as used in the clinical practices - similar MRI scanners (1.5T or 3T) and scanning sequences.

To address the non-technical issues, a robotic needle insertion system in a claustrophobic environment needs to earn the trust of not only the radiologists, but the patients themselves. Thus the system has to be safe in every step, with advance design considerations. Visual confirmation for the radiologists, reduced noise during actuation and sterilization processes can be some areas of interest.

Bibliography

- [1] "Mammogram - Green Imaging," <https://greenimaging.net/mammogram/>, accessed: 2022-06-22.
- [2] L. Ogawa and D. Lindquist, "Dual her2 suppression with lapatinib plus trastuzumab for metastatic inflammatory breast cancer: A case report of prolonged stable disease," *Case Reports in Oncology*, vol. 11, pp. 855–860, 12 2018.
- [3] "Breast ultrasound and catastrophic forgetting," May 2021, [Online; posted 14-May-2021].
- [4] W. Al-Dhabyani, M. Gomaa, H. Khaled, and A. Fahmy, "Dataset of breast ultrasound images," *Data in Brief*, vol. 28, p. 104863, 11 2019.
- [5] U. Fischer, A. Korthauer, F. Baum, S. Luftner-Nagel, and D. Heyden, "Short first-pass mri of the breast," *Acta radiologica*, vol. 32, no. 3, pp. 267–269, 2012.
- [6] P. Gelezhe, I. Blokhin, D. Marapov, and S. Morozov, "Quantitative parameters of mri and 18f-fdg pet/ct in the prediction of breast cancer prognosis and molecular type: an original study," *American journal of nuclear medicine and molecular imaging*, vol. 10, pp. 279–292, 12 2020.
- [7] S. Gao, B. Jia, G. Feng, C. Dong, H. Du, L. Bai, Q. Zhong, Q. ma, M.-S. Zeng, and F. Wang, "First-in-human pilot study of an integrin 6-targeted radiotracer for spect imaging of breast cancer," *Signal Transduction and Targeted Therapy*, vol. 5, 12 2020.
- [8] S. Iranmakani, T. Mortezaazadeh, F. Sajadian, M. Ghaziani, A. Ghafari, D. Khezzloo, and A. Musa, "A review of various modalities in breast imaging: technical aspects and clinical outcomes," *Egyptian Journal of Radiology and Nuclear Medicine*, vol. 51, 12 2020.
- [9] W. Liu, Z. Yang, S. Jiang, D. Feng, and D. Zhang, "Design and implementation of a new cable-driven robot for mri-guided breast biopsy," *The International Journal of Medical Robotics and Computer Assisted Surgery*, vol. 16, 12 2019.

- [10] A. Simmons and K. Hakansson, "Magnetic resonance safety," *Methods in molecular biology (Clifton, N.J.)*, vol. 711, pp. 17–28, 01 2011.
- [11] S. Park, J.-G. Kim, K.-W. Lim, Y. Chae-Hyun, D.-J. Kim, H.-S. Kang, and Y.-H. Jo, "A magnetic resonance image-guided breast needle intervention robot system: overview and design considerations," *International Journal of Computer Assisted Radiology and Surgery*, vol. 12, 02 2017.
- [12] B. Yang, S. Roys, U.-X. Tan, M. Philip, H. Richard, R. Gullapalli, and J. Desai, "Design, development, and evaluation of a master-slave surgical system for breast biopsy under continuous mri," *The International journal of robotics research*, vol. 33, pp. 616–630, 04 2014.
- [13] B. Larson, N. Tsekos, and A. Erdman, "A robotic device for minimally invasive breast interventions with real-time mri guidance," in *Third IEEE Symposium on Bioinformatics and Bioengineering, 2003. Proceedings.*, 2003, pp. 190–197.
- [14] D. Hanahan and R. A. Weinberg, "The hallmarks of cancer," *cell*, vol. 100, no. 1, pp. 57–70, 2000.
- [15] H. Sung, J. Ferlay, R. L. Siegel, M. Laversanne, I. Soerjomataram, A. Jemal, and F. Bray, "Estimates of incidence and mortality worldwide for 36 cancers in 185 countries," *CA: a cancer journal for clinicians*, vol. 71, no. 3, pp. 209–249, 2021. [Online]. Available: <https://doi.org/10.3322/caac.21660>
- [16] N. Zielonke, A. Gini, E. Jansen, A. Anttila, N. Segnan, A. Ponti, Veerus, P. Koning, v. R. H. J., and H. N. T., "Evidence for reducing cancer-specific mortality due to screening for breast cancer in europe: A systematic review," *European journal of cancer and EU-TOPIA consortium (2020)*, vol. 127, pp. 191–206, 2020. [Online]. Available: <https://doi.org/10.1016/j.ejca.2019.12.010>
- [17] "Screening and early detection," Jun 2022. [Online]. Available: <https://www.euro.who.int/en/health-topics/noncommunicable-diseases/cancer/policy/screening-and-early-detection>
- [18] "What is breast cancer screening?" https://www.cdc.gov/cancer/breast/basic_info/screening.htm, accessed: 2022-06-22.
- [19] "Framework for the execution of the dutch breast cancer screening programme," 2021.
- [20] F. Sardanelli, E. Fallenberg, P. Clauser, R. Trimboli, J. Herrero, T. Helbich, and G. Forrai, "Mammography: an update of the eusobi recommendations on information for women," *Insights into imaging*, vol. 8, 11 2016.

- [21] A. Heba, R. Kamal, M. Hanafy, A. Youssef, and L. Hashem, "Comparative study between contrast-enhanced mammography, tomosynthesis, and breast ultrasound as complementary techniques to mammography in dense breast parenchyma," *Egyptian Journal of Radiology and Nuclear Medicine*, vol. 51, 12 2020.
- [22] C. Kuhl, "The changing world of breast cancer: A radiologist's perspective," *Plastic surgical nursing : official journal of the American Society of Plastic and Reconstructive Surgical Nurses*, vol. 36, pp. 31–49, 03 2016.
- [23] "Biopsy - Definition," <https://www.cancer.gov/publications/dictionaries/cancer-terms/def/biopsy>, accessed: 2022-06-22.
- [24] S. Taneja, A. Jena, and A. Mehta, "Technical note: Mri-guided breast biopsy - our preliminary experience," *The Indian journal of radiology & imaging*, vol. 20, pp. 218–20, 08 2010.
- [25] C. Perlet, S. H. Heywang-Kobrunner, A. Heinig, H. Sittek, J. Casselman, I. Anderson, and P. Taourel, "Magnetic resonance-guided, vacuum-assisted breast biopsy: results from a european multicenter study of 538 lesions," *Cancer*, vol. 106, no. 5, pp. 982–990, 2006. [Online]. Available: <https://doi.org/10.1002/cncr.21720>
- [26] V. Groenhuis, F. Siepel, and S. Stramigioli, "Dual-speed mr safe pneumatic stepper motors," 06 2018.
- [27] M. Ghoncheh, Z. Pournamdar, and H. Salehiniya, "Incidence and mortality and epidemiology of breast cancer in the world," *Asian Pacific Journal of Cancer Prevention*, vol. 17, pp. 43–46, 06 2016.
- [28] L. Wang, "Microwave sensors for breast cancer detection," *Sensors*, vol. 18, p. 655, 02 2018.
- [29] D. Grosenick, H. Rinneberg, R. Cubeddu, and P. Taroni, "Review of optical breast imaging and spectroscopy," *J Biomed Opt.*, vol. 21, no. 9, p. 091311, 07 2016.
- [30] "Palpation - Definition," <https://medlineplus.gov/ency/article/002284.htm>, accessed: 2022-06-22.
- [31] "The Breast Exam," <https://stanfordmedicine25.stanford.edu/the25/BreastExam.html>, accessed: 2022-06-22.

- [32] M. T, G. E, R. A. N, H. S, M. A E, and K. M, "Glucosamine conjugated gadolinium (iii) oxide nanoparticles as a novel targeted contrast agent for cancer diagnosis in mri," *Journal of biomedical physics engineering*, vol. 10, no. 1, pp. 25–38, 2020.
- [33] N. K, "Microwave imaging for breast cancer," *IEEE Microwave Magazine*, vol. 12, pp. 78–94, 2011.
- [34] Y. Lu and D. Horsley, "Modeling, fabrication, and characterization of piezoelectric micromachined ultrasonic transducer arrays based on cavity soi wafers," *Journal of Microelectromechanical Systems*, 01 2015.
- [35] E. Morris and L. Liberman, *Breast MRI: Diagnosis and Intervention*, 01 2005.
- [36] "Phyiscis of Mri - Detailed?" https://my-ms.org/mri_physics.htm, accessed: 2022-06-24.
- [37] S. Bhole and E. I. Neuschler, "Mri-guided breast interventions," *Applied Radiology*, 2015.
- [38] J. S. Drukteinis, B. P. Mooney, C. I. Flowers, and R. A. Gatenby, "Beyond mammography: new frontiers in breast cancer screening." *The American journal of medicine*, vol. 126, no. 6, pp. 472–479, 2013.
- [39] B. Tromberg, B. Pogue, K. Paulsen, A. Yodh, D. Boas, and A. Cerussi, "Assessing the future of diffuse optical imaging technologies for breast cancer management," *Medical physics*, vol. 35, pp. 2443–51, 06 2008.
- [40] F. Britto and V. R. Shetty J, "Biopsy-an overview," 10 2020.
- [41] S. Versaggi and A. De Leucio, *Breast Biopsy*, 06 2020.
- [42] M. Z. Mahmoud, M. Aslam, M. Alsaadi, M. Fagiry, and B. Alonazi, "Evolution of robot-assisted ultrasound-guided breast biopsy systems," vol. 11, 01 2018.
- [43] "Ultrasound-guided breast biopsy," <https://www.radiologyinfo.org/en/info/breastbius>, accessed: 2022-06-24.
- [44] Y. Kang and Y. Kim, "Comparison of needle aspiration and vacuum-assisted biopsy device for the ultrasound-guided drainage of lactating breast abscess," *Ultrasonography*, vol. 35, 12 2015.
- [45] V. Groenhuis, "Robotic systems for breast biopsy using MRI and Ultrasound imaging: Optimal guidance to target lesion in deformable tissue," Ph.D. dissertation, University of Twente, Netherlands, January 2022.

- [46] “Mri-Guided Breast Biopsy,” <https://www.radiologyinfo.org/en/info/breastbimr#:~:text=Magnetic%20resonance%2D%20or%20MR%2Dguided,leaves%20little%20to%20no%20scarring.>, accessed: 2022-06-24.
- [47] R. Gassert, A. Yamamoto, D. Chapuis, L. Dovat, H. Bleuler, and E. Burdet, “Actuation methods for applications in mr environments,” *Concepts in Magnetic Resonance Part B: Magnetic Resonance Engineering*, vol. 29, pp. 191–209, 10 2006.
- [48] K. Chinzei, R. Kikinis, and F. A. Jolesz, “Mr compatibility of mechatronic devices: Design criteria,” in *MICCAI*, 1999.
- [49] R. Gassert, A. Yamamoto, D. Chapuis, L. Dovat, H. Bleuler, and E. Burdet, “Actuation methods for applications in mr environments,” *Concepts in Magnetic Resonance Part B: Magnetic Resonance Engineering*, vol. 29, pp. 191–209, 10 2006.
- [50] “Mr Safe– MR Conditional. who,what, why, when, how,” <http://synthes.vo.llnwd.net/o16/Mobile/Synthes%20International/KYO/Trauma/PDFs/036.001.075.pdf>, accessed: 2022-06-25.
- [51] Y. Zhang, M. Lu, and H. Du, “Kinematics analysis and trajectory planning for a breast intervention robot under mri environment,” 10 2017, pp. 237–242.
- [52] D. Navarro-Alarcon, S. Singh, T. Zhang, H. Chung, K. W. Ng, M. CHOW, and Y. Liu, “Developing a compact robotic needle driver for mri-guided breast biopsy in tight environments,” *IEEE Robotics and Automation Letters*, vol. 2, pp. 1–1, 01 2017.
- [53] V. Groenhuis, F. Siepel, and S. Stramigioli, “Miniaturization of mr safe pneumatic rotational stepper motors,” 11 2019, pp. 7150–7156.
- [54] V. Groenhuis and S. Stramigioli, “Laser-cutting pneumatics,” *IEEE/ASME Transactions on Mechatronics*, vol. 21, pp. 1–1, 01 2015.
- [55] M. Abdelaziz, V. Groenhuis, J. Veltman, F. Siepel, and S. Stramigioli, “Controlling the stormram 2: An mri-compatible robotic system for breast biopsy,” 05 2017, pp. 1746–1753.
- [56] V. Groenhuis and S. Stramigioli, “Rapid prototyping high-performance mr safe pneumatic stepper motors,” *IEEE/ASME Transactions on Mechatronics*, vol. PP, pp. 1–1, 05 2018.

- [57] V. Groenhuis, J. Veltman, F. Siepel, and S. Stramigioli, "Stormram 3: A magnetic-resonance-imaging-compatible robotic system for breast biopsy," *IEEE Robotics Automation Magazine*, vol. PP, pp. 1–1, 05 2017.
- [58] Y. Patel and G. P M, "Parallel manipulators applications—a survey," *Modern Mechanical Engineering*, vol. 2, pp. 57–64, 08 2012.
- [59] V. Groenhuis, F. Siepel, J. Veltman, J. Zandwijk, and S. Stramigioli, "Stormram 4: An mr safe robotic system for breast biopsy," *Annals of Biomedical Engineering*, vol. 46, 05 2018.
- [60] V. Groenhuis, F. Siepel, and S. Stramigioli, "Dual-speed mr safe pneumatic stepper motors," Jun. 2018, robotics: Science and Systems 2018, RSS 2018 ; Conference date: 26-06-2018 Through 30-06-2018. [Online]. Available: <http://roboticsconference.org/>
- [61] A. Steinmann, R. J. Stafford, G. Sawakuchi, Z. Wen, L. Court, C. Fuller, and D. Followill, "Developing and characterizing mr/ct visible materials used in qa phantoms for mrgt systems," *Medical Physics*, vol. 45, 11 2017.
- [62] M. W. Spong, S. Hutchinson, and M. Vidyasagar, *Robot Modeling and Control*. United States: John Wiley and Sons Ltd, 2020, pp. 75–99.
- [63] S. Kucuk and Z. Bingul, *Robot Kinematics: Forward and Inverse Kinematics*, Dec 2006.
- [64] —, *Robot Kinematics: Forward and Inverse Kinematics*, Dec 2006.
- [65] "Industrial robot functionality and coordinate systems," <https://www.tthk.ee/inlearcs/industrial-robot-functionality-and-coordinate-systems/#:~:text=The%20work%20volume%20or%20work,physical%20size%20of%20the%20links.,> accessed: 2022-06-27.
- [66] "Air solenois valve," <https://nl.farnell.com/stmicroelectronics/tip120/transistor-npn-60v-5a-to-220/dp/9804005>, accessed: 2022-06-27.
- [67] "Tip120 transistors," https://www.festo.com/us/en/a/525101/?q=~:sortByFacetValues-asc~:CC_Type_of_directional_control_valve_C_FP_GLOBAL~:CC_Type_of_directional_control_valve.B~:CC_Valve_function_C_FP_GLOBAL~:CC_Valve_function.M52, accessed: 2022-06-27.
- [68] P. Pedamkar, "Types of Research Methodology," <https://www.educba.com/types-of-research-methodology/>, accessed: 2022-06-28.

- [69] C. Moore and D. Bell, "Segmentation - reference article," *Radiopaedia.org*, 01 2020.
- [70] J. Gilbert, G. Wheeler, G. Richardson, S. Herder, G. Mick, E. Watts, K. Gyarteng-Dakwa, C. Kenney, and P. Broughton, "Guidance of magnetic resonance imaging and placement of skin-marker localization devices," *Journal of neurosurgical sciences*, vol. 55, pp. 85–8, 06 2011.
- [71] E. S.p.a, "G-scan User Manual," https://eifu.esaote.com/fileadmin/Manuals/MRI/english/G-scan_User_Manual.pdf, accessed: 2022-06-28.
- [72] S.-E. Song, N. Cho, I. Iordachita, P. Guion, G. Fichtinger, A. Kaushal, K. Camphausen, and L. Whitcomb, "Biopsy needle artifact localization in mri-guided robotic transrectal prostate intervention," *IEEE transactions on bio-medical engineering*, vol. 59, pp. 1902–11, 04 2012.
- [73] A. Fedorov, R. Beichel, J. Kalpathy-Cramer, J. Finet, J.-C. Fillion-Robin, S. Pujol, C. Bauer, D. Jennings, F. Fennessy, M. Sonka, J. Buatti, S. Aylward, J. Miller, S. Pieper, and R. Kikinis, "3d slicer as an image computing platform for the quantitative imaging network," *Magnetic resonance imaging*, vol. 30, pp. 1323–41, 07 2012.
- [74] C. Pinter, A. Lasso, and G. Fichtinger, "polymorph segmentation representation for medical image computing," *Computer Methods and Programs in Biomedicine*, vol. 171, pp. 19–26, 2019.
- [75] "Coordinate systems - 3D Slicer," https://www.slicer.org/wiki/Coordinate_systems, accessed: 2022-06-28.
- [76] MATLAB, *version 9.11 (R2021b)*. Natick, Massachusetts: The MathWorks Inc., 2021.
- [77] M. 2020b, "estimategeometrictransform3d," <https://www.mathworks.com/help/vision/ref/estimategeometrictransform3d.html>, 2020, accessed on : 28-05-2022.
- [78] S. Kulkarni, D. Bormane, and S. Nalbalwar, "Ransac algorithm for matching inlier correspondences in video stabilization," *Advances in Image and Video Processing*, vol. 5, 02 2017.
- [79] M. 2020b, "procrustes," [https://www.mathworks.com/help/stats/procrustes.html#:~:text=procrustes%20computes%20the%20distance%20using,X%2Dmean\(X\)\).](https://www.mathworks.com/help/stats/procrustes.html#:~:text=procrustes%20computes%20the%20distance%20using,X%2Dmean(X)).), 2020, accessed on : 28-05-2022.

- [80] J. Lawrence, J. Bernal, and C. Witzgall, "A purely algebraic justification of the kabsch-umeyama algorithm," *Journal of research of the National Institute of Standards and Technology*, vol. 124, 10 2019.
- [81] Arduino.cc, "Arduino uno," <https://store.arduino.cc/products/arduino-uno-rev3>, accessed on : 28-05-2022.
- [82] U. BV, "Ultimaker s5," <https://ultimaker.com/3d-printers/ultimaker-s5>, the Netherlands. Accessed on : 28-05-2022.
- [83] "Ziekenhuisgroep Twente (ZGT)," <https://www.zgt.nl/>, accessed: 2022-07-02.
- [84] C. Sinai, "Mr guided breast needle-core biopsy procedure information," <https://www.cedars-sinai.org/programs/imaging-center/exams/mri/mr-breast-biopsy/information.html>, accessed: 2022-07-02.
- [85] L. Liberman, G. Mason, E. Morris, and D. Dershaw, "Does size matter? positive predictive value of mri-detected breast lesions as a function of lesion size," *AJR. American journal of roentgenology*, vol. 186, pp. 426–30, 03 2006.

Appendix A

The following chapter contains the additional resources and data, which add value to the study conducted with the Sunram 7. These are used through the entirety of the study, and hence this chapter provides an overview of the structures explained in previous numerous sections.

A.1 Breast phantoms

The breast phantoms used for the the validation and experimentation of the study are shown in figure A.1.

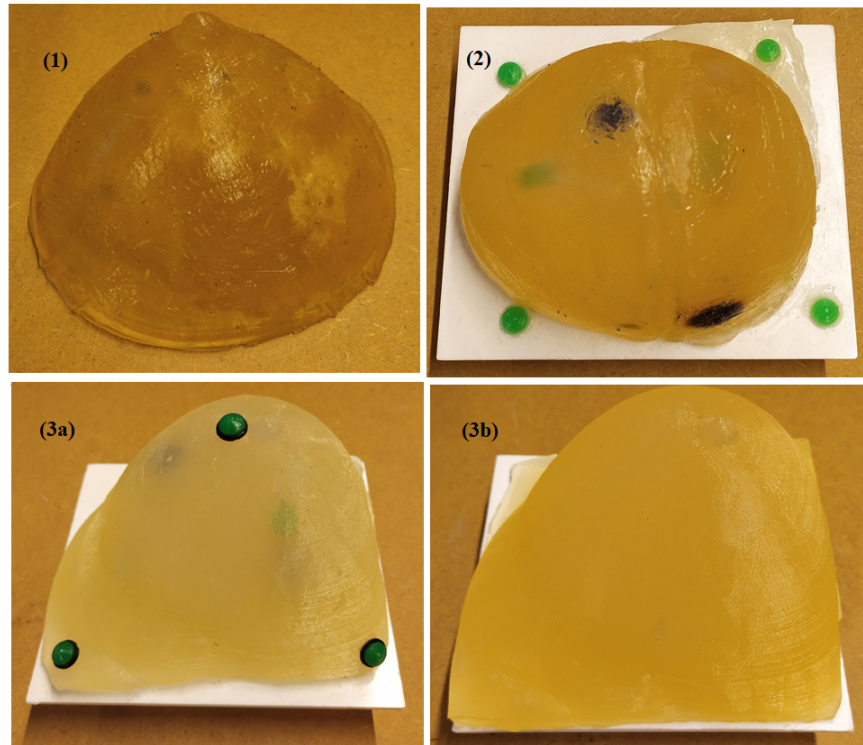


Figure A.1: Different breast phantoms

A.2 MRI scanning sequences

The MRI imaging modality had to be studied to choose the a suitable scanning sequence for this study. As mentioned in section 4.2.2, different sequences were tried and the scanned image obtained are shown in figure A.2.

A.3 Segmentation

The 3D Slicer software package, along with the many modules and extensions, enabled the successful and accurate segmentation of the breast phantom, the lesions within, the fiducial markers and the target markers. The different markers are color coded, to help differentiate them - the 8 fiducial markers are in blue, the 3 tall target markers are in red and the 2 short markers are magenta/pink in colour, as shown in figure A.3.

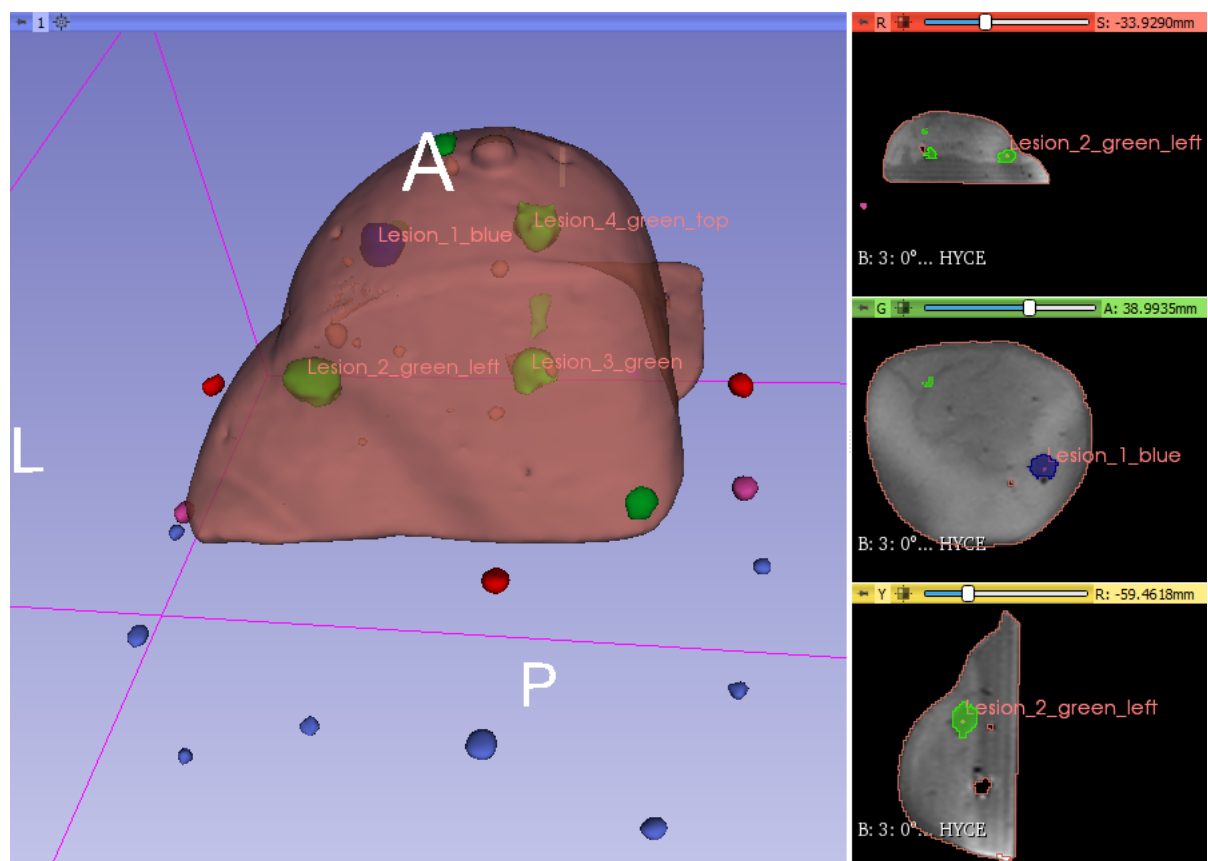


Figure A.3: 3D Slicer window containing the segmented breast phantom, lesions, 8 fiducial markers(blue) and 5 target markers(3 x tall-red,2 x short-pink/magenta)

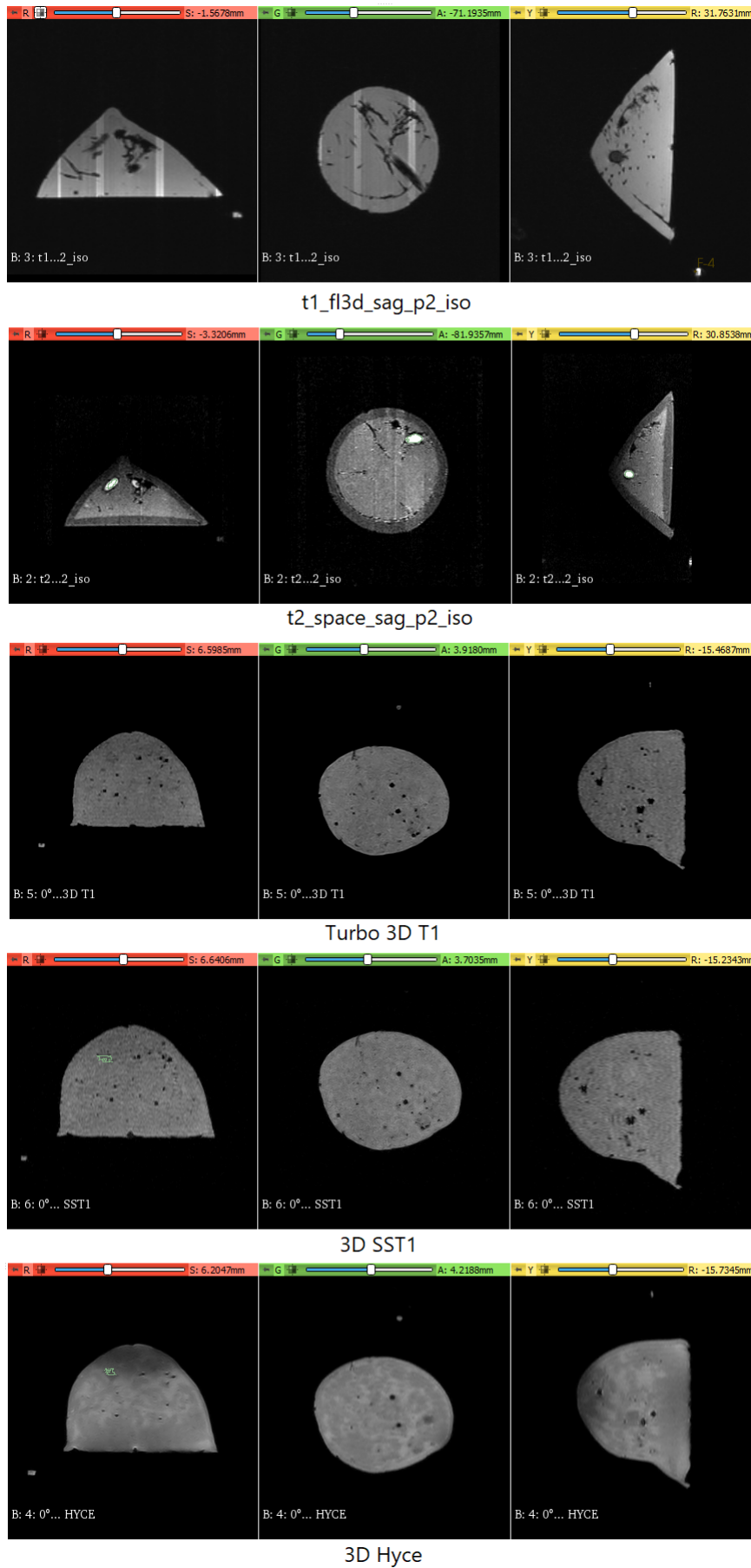


Figure A.2: Different MRI scanning sequences

A.4 Homogeneous transformation matrix

As mentioned in section 3.2.1 ,the final transformation matrix from the base to the needle tip is ¹ :

$$T_N^B = \begin{bmatrix} a_{11} & a_{12} & a_{13} & a_{14} \\ a_{21} & a_{22} & a_{23} & a_{24} \\ a_{31} & a_{32} & a_{33} & a_{34} \\ 0 & 0 & 0 & 1 \end{bmatrix} \quad (\text{A.1})$$

where , T_N^B denotes the transformation from Base to the Needle tip and,

$$a_{11} = \cos(\theta_1 + \theta_2) \quad (\text{A.2})$$

$$a_{12} = -\sin(\theta_1 + \theta_2) \cdot \sin(\theta_3 - \theta_4) \quad (\text{A.3})$$

$$a_{13} = -\sin(\theta_1 + \theta_2) \cdot \cos(\theta_3 - \theta_4) \quad (\text{A.4})$$

$$\begin{aligned} a_{14} = & 228 \cdot \sin(\theta_1) - 30 \cdot \sin(\theta_1 + \theta_2 - \theta_3) - \\ & 15 \cdot \cos(\theta_1 + \theta_2 + \theta_3 - \theta_4)/2 + 15 \cdot \cos(\theta_1 + \theta_2 - \theta_3 + \theta_4)/2 - \\ & 125 \cdot \sin(\theta_1 + \theta_2 + \theta_3 - \theta_4)/2 - 125 \cdot \sin(\theta_1 + \theta_2 - \theta_3 + \theta_4)/2 - \\ & 30 \cdot \sin(\theta_1 + \theta_2 + \theta_3) + (142.58 \cdot \sin(\text{atan}(0.1588) + \theta_1 + \theta_2))/2 - \\ & (d_5 \cdot \sin(\theta_1 + \theta_2 + \theta_3 - \theta_4))/2 - (d_5 \cdot \sin(\theta_1 + \theta_2 - \theta_3 + \theta_4))/2 \end{aligned} \quad (\text{A.5})$$

$$a_{21} = \sin(\theta_1 - \theta_2) \quad (\text{A.6})$$

$$a_{22} = \cos(\theta_1 + \theta_2) \cdot \sin(\theta_3 - \theta_4) \quad (\text{A.7})$$

$$a_{23} = \cos(\theta_1 + \theta_2) \cdot \cos(\theta_3 - \theta_4) \quad (\text{A.8})$$

$$\begin{aligned} a_{24} = & 30 \cdot \cos(\theta_1 + \theta_2 - \theta_3) - 228 \cdot \cos(\theta_1) + \\ & (125 \cdot \cos(\theta_1 + \theta_2 + \theta_3 - \theta_4))/2 + (125 \cdot \cos(\theta_1 + \theta_2 - \theta_3 + \theta_4))/2 - \\ & (15 \cdot \sin(\theta_1 + \theta_2 + \theta_3 - \theta_4))/2 + (15 \cdot \sin(\theta_1 + \theta_2 - \theta_3 + \theta_4))/2 + \\ & 30 \cdot \cos(\theta_1 + \theta_2 + \theta_3) - (142.58 \cdot \cos(\text{atan}(0.1558) + \theta_1 \\ & + \theta_2))/2 + (d_5 \cdot \cos(\theta_1 + \theta_2 + \theta_3 - \theta_4))/2 + (d_5 \cdot \cos(\theta_1 + \theta_2 - \theta_3 + \theta_4))/2 \end{aligned} \quad (\text{A.9})$$

¹all angles are in radians

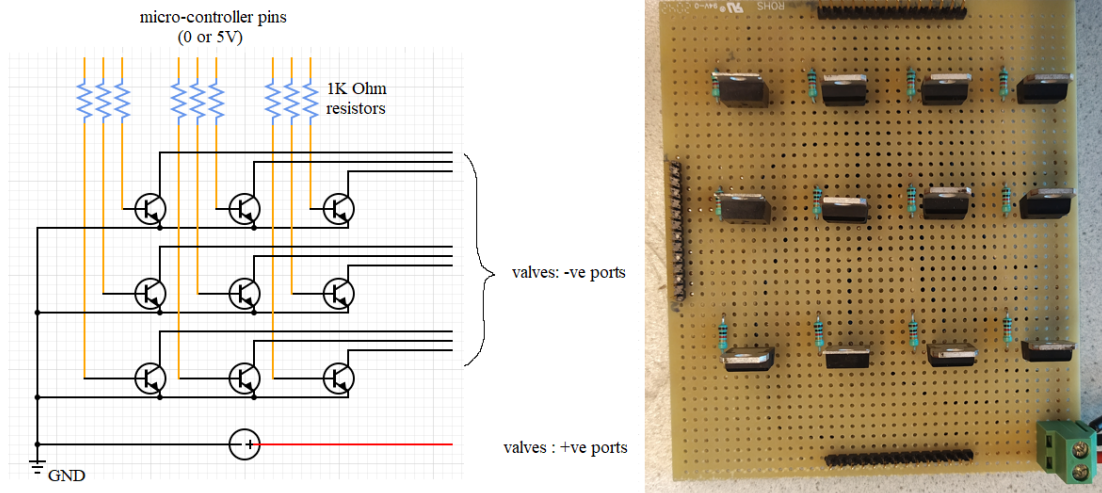


Figure A.4: Left: The power management circuit design. Right: Soldered circuit board with TIP120 transistors

$$a_{31} = 0 \quad (\text{A.10})$$

$$a_{32} = -\cos(\theta_3 - \theta_4) \quad (\text{A.11})$$

$$a_{33} = \sin(\theta_3 - \theta_4) \quad (\text{A.12})$$

$$a_{34} = 60 \cdot \sin(\theta_3) + 15 \cdot \cos(\theta_3 - \theta_4) + 125 \cdot \sin(\theta_3 - \theta_4) + d5 \cdot \sin(\theta_3 - \theta_4) + 26 \quad (\text{A.13})$$

A.5 Interface circuit

The power control circuit fabricated enables the Arduino to control the pneumatic valves, thus providing a digital control to the Sunram 7. The basic circuit layout and the soldered PCB along with the TIP120 transistors are shown in figure A.4. This control circuit was used for all experiments outside the MRI room.

An extensive controller, designed at RAM for Sunram 7-like pneumatic robots is shown in figure A.5 This controller is used for research purposes and can work stand-alone. This was also used to control the Sunram 7 inside the MRI room.

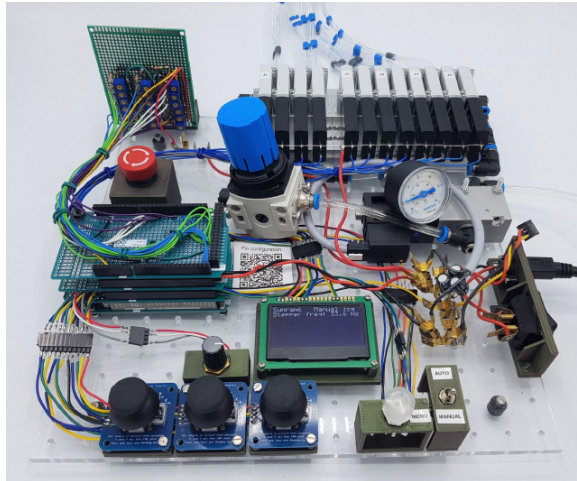


Figure A.5: Controller designed for Sunram 7

A.6 Sunram 7 system

Shown in figure A.6, all components of the Sunram 7 are highlighted. The 24V DC power source (a) provides the electrical energy needed to actuate the pneumatic valves (b), through the interface circuit made from TIP120 transistors (c) and controlled via Arduino Uno (d). The pressure regulator (e) helps set the compressed air pressure supplied through the tubes (i), which actuates the Sunram 7 robot (f) on its base frame attached to the grid-board. Target pillars (g) and breast phantoms (h) are instruments used for different tests described in this study. Figure A.7 left show the long and short markers used for checking the target registration error and the right shows the different target pillars fabricated.

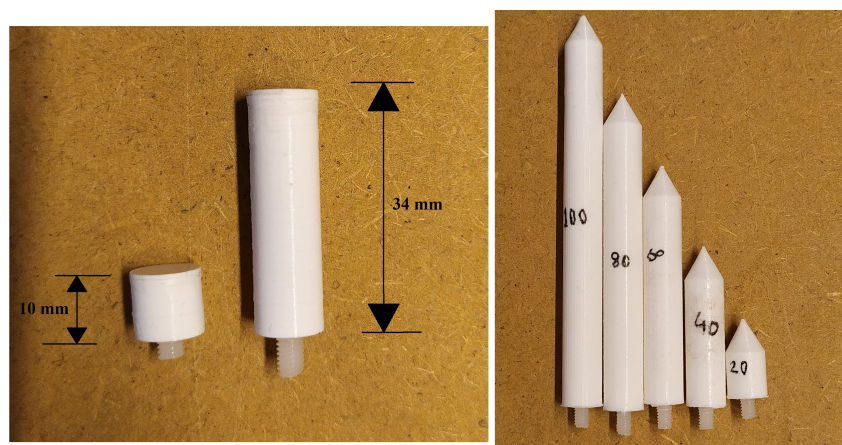


Figure A.7: Left: Long and short markers for TRE. Right: target pillars for tests

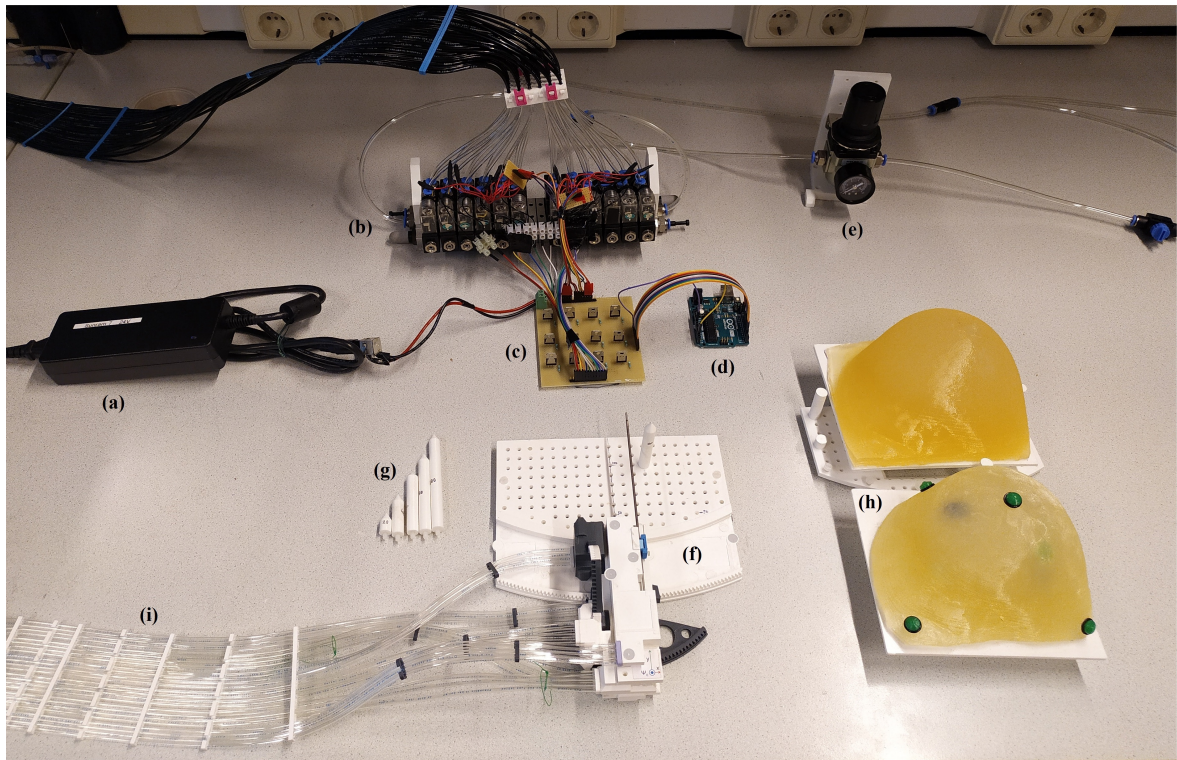


Figure A.6: The complete Sunram 7 system

A.7 Needle targeting - in air : Setup and output

The experimental setup for studying the targeting accuracy of the Sunram 7 and the obtained 'punctured' target filled graph sheet is shown below :

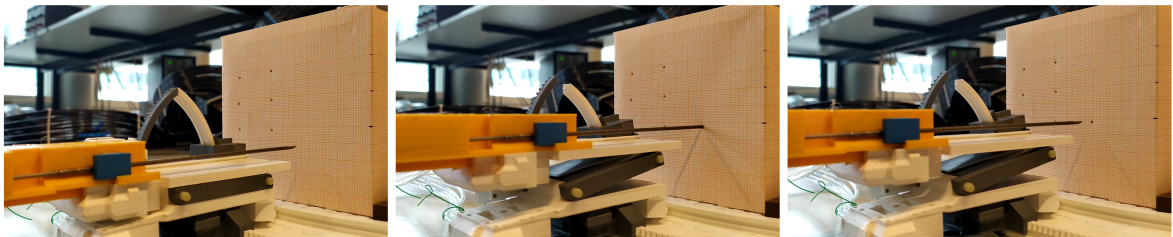


Figure A.8: Setup: To study Sunram 7's needle targeting accuracy in free air - Before insertion(left), during insertion/targeting(center) and after making a hole at the target location(right)

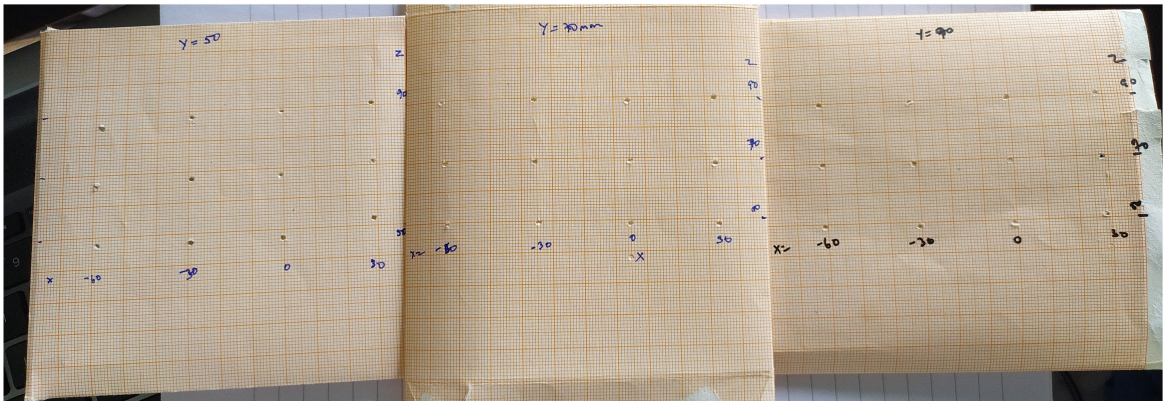


Figure A.9: Target sheets, at three different y planes, with 'punctures'

A.8 Accuracy evaluation - MR environment

The experimental setup in the MR-room was arranged as shown in figure A.10. The breast phantom (A), is made from plastisol, which contains stiff PVC 'lesions'. The Sunram 7 (B), along with the biopsy needle is fixed at the zero position through visual calibration and then the joint 5 is actuated by a fixed amount (200 steps) in the negative y direction. The entire setup is then placed inside a breast coil (C), which is part of the Esaote 0.25T scanner.

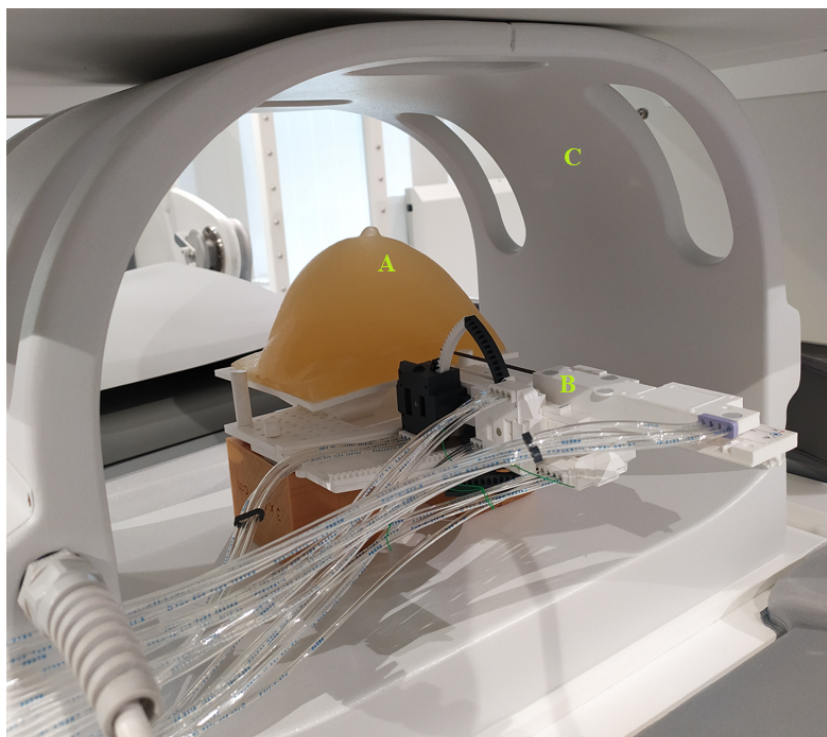


Figure A.10: Sunram 7 and breast phantom setup inside the MR room

The biopsy samples obtained by the Sunram 7, described in section 5.6 is shown in figure A.11. The attachment designed to prevent the bending of needle during needle insertion is shown in figure A.12.

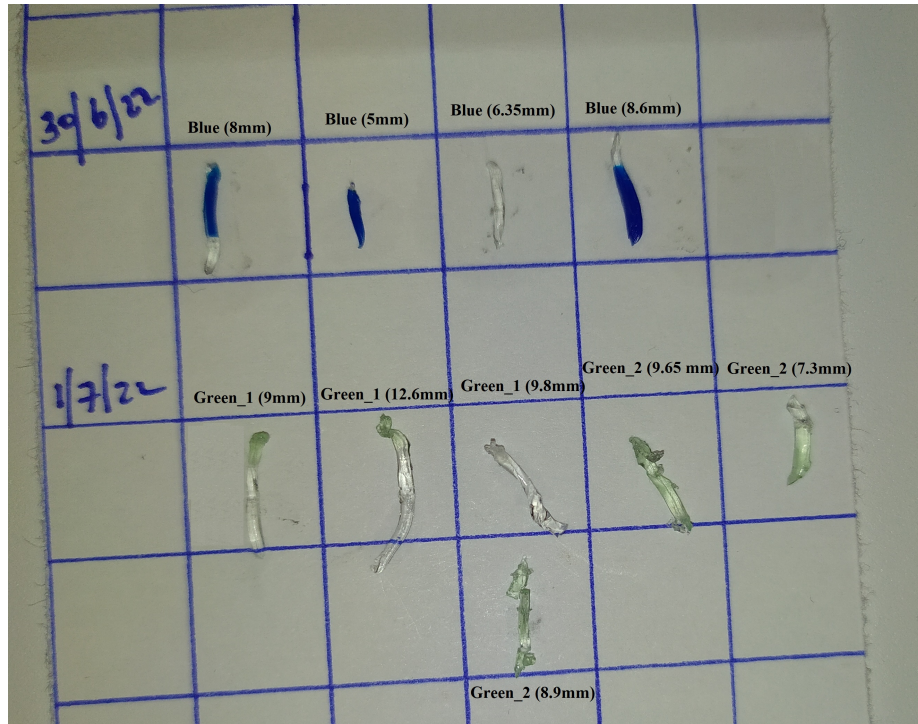


Figure A.11: Biopsy sample outputs for 3 lesions

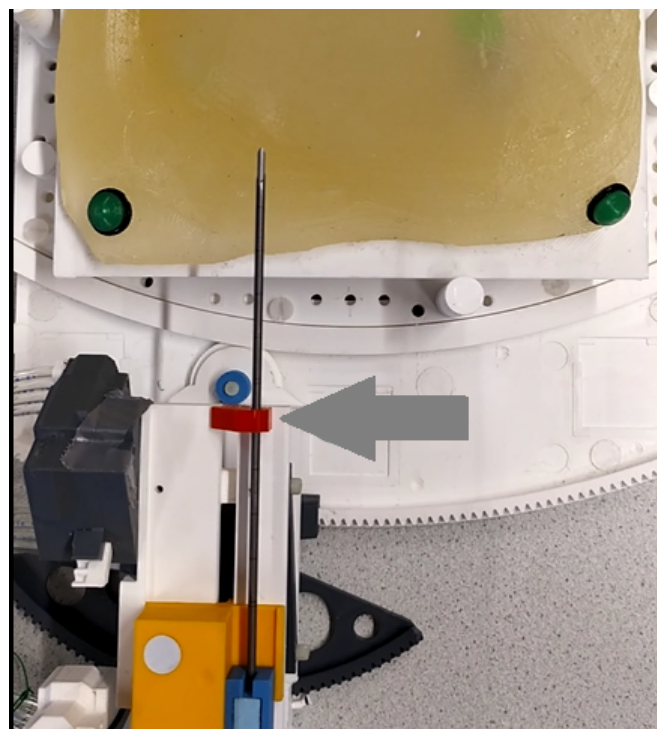


Figure A.12: The red attachment designed to prevent needle bending